nature nanotechnology

Article

https://doi.org/10.1038/s41565-026-02198-x

Programmed synthesis of mesoporous protein crystals in cellular reactors

Received: 2 October 2025

Accepted: 11 May 2026

Published online: 15 June 2026

Check for updates

Hongru Yang[1], Dian-Zhao Lin[2], Zhe Li[3,8], Yuqing Yan[1,4], Zuo-Han Zhao[1], Byeongdu Lee[5], Chang Woo Song[1,4], Shunzhi Wang[3], Jiaxi Lu[1,4], Yimei Wang[1,4], Yongzhi Sun[1,4], Ken Livi[1], David Baker[3], Yayuan Liu[2] ✉ & Dingchang Lin[1,4,6,7] ✉

Protein crystals are naturally derived mesoporous materials with versatile structures and physicochemical properties. Here we introduce an intracellular synthesis platform that enables controllable and programmable protein crystallization. In live cells, we show that, after initial nucleation, steady protein expression governs crystal growth, yielding predictable, tunable dynamics in live cells. Exploiting this feature, we combined HaloTag and click chemistries to achieve modular, programmable immobilization of diverse guest materials with spatial patterning down to ~100 nm resolution. We further demonstrated the sequential release of immobilized materials in physiologically relevant fluids. As a proof of concept, we programmed particles to carry human fibroblast growth factors in distinct layers, which elicited designed oscillatory Akt signalling patterns in cell culture. This work outlines a programmable method for producing mesoporous materials, with possible applications in catalysis and biomedicine.

Protein crystals are a distinct class of mesoporous materials, characterized by their ordered lattices, structural diversity and intrinsic biological origin[1–4]. During crystallization, proteins self-assemble into long-range, three-dimensional (3D) lattices that inherently contain interconnected mesopores[5–7]. The diversity of protein sequences, conformations and interfacial properties creates a limitless landscape of possible structures. Recent advances in protein design have further enabled de novo crystals with tunable porosity and pore dimensions, expanding the design potential of crystalline mesoporous protein materials[8–10]. Their biological nature also provides inherent biofunctionality, biodegradability and biocompatibility, while genetic and biochemical engineering allows facile modification and functionalization[11–19]. Together, these attributes make protein crystals promising applications in biology, biomedicine and beyond[20,21].

Protein crystals are conventionally synthesized via in vitro processes, where proteins are purified from microbial expression systems, concentrated and crystallized under meticulously optimized conditions[22]. Like inorganic crystallization, these processes initiate in static, supersaturated environments, where nuclei form and grow through continuous building-block consumption within a metastable zone until equilibrium is reached[23,24]. This kinetically driven process limits control over nucleation and growth, causes batch-to-batch variability and potentially traps defects. The emerging intracellular crystallization offers a scalable and cost-effective alternative by bypassing protein purification and guest loading[4,25], but its broader potential remains underexplored.

Here, we established the predictable and controllable synthesis of computationally designed protein crystals within live mammalian cells.

[1]Department of Materials Science and Engineering, Whiting School of Engineering, Johns Hopkins University, Baltimore, MD, USA. [2]Department of Chemical and Biomolecular Engineering, Whiting School of Engineering, Johns Hopkins University, Baltimore, MD, USA. [3]Institute for Protein Design, University of Washington, Seattle, WA, USA. [4]Institute for NanoBioTechnology, Whiting School of Engineering, Johns Hopkins University, Baltimore, MD, USA. [5]X-ray Science Division, Advanced Photon Source, Argonne National Laboratory, Argonne, Lemont, IL, USA. [6]Kavli Neuroscience Discovery Institute, Johns Hopkins University, Baltimore, MD, USA. [7]Center for Cell Dynamics, School of Medicine, Johns Hopkins University, Baltimore, MD, USA. [8]Present address: Department of Biomedical Engineering, Southern University of Science and Technology, Shenzhen, China. ✉e-mail: yayuanliu@jhu.edu; dclin@jhu.edu

https://doi.org/10.1038/s41565-026-02198-x

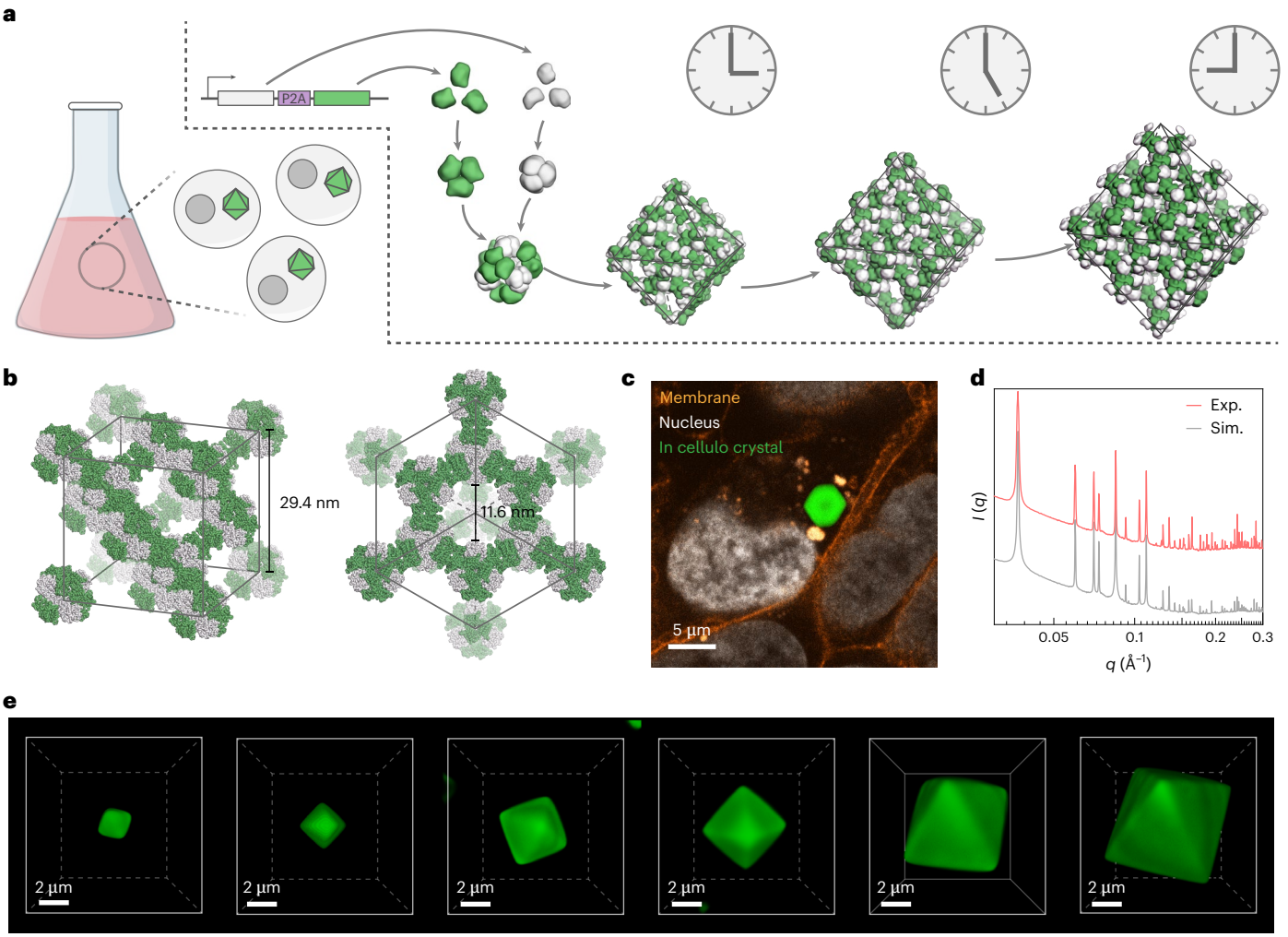

Fig. 1 | Intracellular synthesis of computationally designed protein crystals. **a**, Schematic of intracellular synthesis of protein crystals. Cells carrying the genes of the crystal building blocks were cultured to produce crystals intracellularly. As cells supply the building blocks in a steady and predictable manner, crystal growth over time can be predicted and controlled. **b**, Perspective view (left) and [111] projection (right) of the computational model of FC1m structure. **c**, Fluorescence image showing the crystallization of FC1m in a HEK293T cell. Experiments were independently repeated five times with similar results. Green, FC1m crystal; grey, nuclei; orange, plasma membrane. **d**, SAXS profile of intracellular FC1m (red) compared with the simulated profile (grey). Exp., experimental data; Sim., simulated profile; *q*, scattering vector. **e**, Reconstructed 3D images showing that intracellular FC1m maintains an octahedral shape throughout different stages of growth.

Live cells act as isolated, uniform microreactors that confine nucleation and growth while continuously supplying building blocks to sustain post-equilibrium growth (Fig. 1a). We developed a mathematical model that accurately describes intracellular growth dynamics. Leveraging this predictability, we programmed HaloTag-mediated installation of orthogonal click-chemistry ligands at defined radial positions, creating nanoscale layered patterns with sharp boundaries, tunable spacings and specific reactivity. Diverse guests, including inorganic particles, proteins and organic molecules, were subsequently immobilized into designated layers, yielding complex structural and compositional patterns of up to 4 distinct guests and 11 layers. These layer-patterned crystals dissolved sequentially in physiological fluids. Programmed crystals loaded with basic fibroblast growth factor (bFGF) in defined layers induced oscillatory Akt signalling in live cells, highlighting their potential for programmed drug release.

Intracellular synthesis of protein crystals with high porosity

Spontaneous crystallization in live cells is rare and limited to few known proteins[26], underscoring the need for robust, on-demand methods to generate intracellular protein crystals. Advances in protein design now enable protein construction with accurate structures[27–29], and a recent hierarchical strategy has generated in vitro crystals with broadly tunable porosity and pore size, providing a foundation for designing intracellular crystals. Exploiting this principle, we constructed three distinct two-component lattices and diversified them by mutating binding residues within extendable interfaces (Fig. 1b and Extended Data Fig. 1a,c). The resulting variants were screened within HEK293T cells via transient transfection. The plasmid encoding the two building blocks of each variant was constructed using a P2A domain for equimolar expression (Extended Data Fig. 1e). Variants that formed intracellular assemblies were identified in all three lattices (Fig. 1c and Extended Data Fig. 1b,d), probably reflecting the design accuracy and the low likelihood of non-specific interactions with endogenous proteins.

Among the variants, we selected FC1 for further optimization. FC1 crystallizes into a high-symmetry cubic lattice (Fig. 1b), with interconnected ~11.6-nm pores and ~85% porosity, well suited for immobilizing diverse nanomaterials (Supplementary Fig. 1). Structural analysis identified interfacial T55 and I58 as critical for lattice extension: T55

engages in hydrogen bonding with D62 and R123, while I58 forms a hydrophobic core. We systematically mutated both sites and expressed each variant in HEK293T cells.

Substituting T55 with positively charged residues substantially enhanced intracellular crystallization, where stronger positive charge increases crystal yield (Extended Data Fig. 2), probably through electrostatic interactions with D62. By contrast, I58 tolerated substitution with other hydrophobic residues or cysteine without notably compromising crystallization (Extended Data Fig. 3).

Among the tested variants, T55R (FC1m) exhibited the most efficient intracellular crystallization and was selected for further characterization. Small-angle X-ray scattering (SAXS) analysis of extracted, intracellularly formed FC1m closely matched the computationally designed lattice model (Fig. 1d and Supplementary Fig. 2). FC1m crystals consistently adopted an octahedral morphology throughout distinct growth stages, indicating high crystallinity and preferential exposure of the low-energy {111} facets (Fig. 1e). Given the favourable properties, FC1m was used as our model system, while other variants remain promising for future optimization.

Predictable and controllable crystallization in live cells

We next investigated whether cellular reactors support predictable and controllable crystallization. Unlike conventional in vitro approaches where growth ceases upon building-block depletion, intracellular crystals exhibit a second steady-growth phase driven by the sustained, predictable and controllable synthesis of building blocks (Supplementary Fig. 3a).

We established a mathematical model for the steady-state phase (Methods). In live cells, newly synthesized building blocks either remain soluble, undergo degradation or incorporate into crystals (Supplementary Fig. 3b). At steady state, the concentration of soluble building blocks remains constant, resulting in a constant degradation rate under first-order kinetics. Assuming constant-rate building-block synthesis when transcription, translation and mRNA degradation reach equilibrium, the incorporation rate into crystals should also remain constant. As FC1 grow as perfect octahedra, we derived the edge length a_t as a function of time t: $a_t = (K_0 t + C)^{1/3}$ (1), where K_0 and C are constants (Methods).

We assessed the model's accuracy by mapping and simulating FC1m growth. To avoid variability from transient transfection, we generated a clonal HEK293T cell line stably expressing FC1m (Supplementary Fig. 4). A ~34-kDa HaloTag was fused to the N terminal of a subset of FC1m-A building blocks through a flexible $(GGS)_6$ linker, enabling chemical functionalization and fluorescent visualization[30]. To limit pore occupancy, untagged and HaloTag-fused building blocks were coexpressed at a ~7:2 molar ratio, yielding crystals with ~35 mol% HaloTag-fused A chains (Supplementary Fig. 5). Expression was induced with doxycycline (DOX) using a Tet-ON system[31], and growth was tracked by time-lapse imaging over 64 h. Size-distribution dynamics were quantified by segmenting and analysing all crystals in each frame (Supplementary Fig. 6). A substantial number of crystals was detected within 5 h post-induction, suggesting a low nucleation energy barrier. The early and synchronous nucleation limits pre-equilibrium crystal growth, thereby preserving the capacity for the controllable phase. As growth progressed, a bimodal distribution emerged, probably from the nucleation of new crystals after cell division (Fig. 2a). As most cells nucleate only one crystal (Fig. 2b), division randomly partitions the crystal to one daughter cell, leaving the other crystal-free and prone to further nucleation.

To further characterize growth dynamics, we analysed the population of larger crystals in each scene (Fig. 2a, yellow), corresponding to those from initial nucleation. The volume index, derived from the segmented area (Methods), increased linearly with time ($R^2 = 0.988$), closely matching the mathematical model (Fig. 2c, red, and Supplementary Movie 1). Linear growth persisted over 60 h, and remained stable throughout early passages (≤P12), whereas later passages (P20) showed slower growth (Supplementary Fig. 7). Therefore, only cells at passage 10 or lower were used in this study.

We then modulated the growth rate via tuning building-block expression, achieved by clonal cell lines with varied FC1m gene copy numbers. In addition to the original fast-growing line, we generated medium and slow lines, both showing linear growth with R^2 values of 0.995 and 0.978, respectively (Fig. 2c, violet and orange). Their nucleation onset, however, was delayed to ~12 and ~17 h post-induction, reflecting the longer time needed to reach supersaturation threshold for nucleation (Fig. 2c). The three cell lines exhibited distinct growth rates across a broad range (Fig. 2d). This was further validated by tracking the growth of individual crystals, where similar growth kinetics were observed (Extended Data Fig. 4 and Supplementary Movie 2). Taken together, these results show that intracellular crystal synthesis is both predictable and controllable.

Structural stability and programmability of FC1m crystal

To spatially program FC1m growth, minimal building-block exchange is essential. Some porous materials, such as metal–organic frameworks, exhibit dynamic skeletons and tend to form homogeneous structures[32]. Here, we quantified the exchange rate of FC1m building blocks by introducing spatial heterogeneity and monitoring homogenization over prolonged incubation. Specifically, heterogeneity was introduced by sequentially staining growing HaloTag-labelled crystals using HaloTag-ligand-conjugated Janelia Fluor (JF) dyes of distinct colours[33–35]. The layer-patterned crystals were extracted, incubated in phosphate-buffered saline (PBS) supplemented with saturated building blocks (Supplementary Fig. 8), and monitored for pattern sharpness over 28 days (Fig. 2e–h and Supplementary Fig. 9).

Initially, extracted crystals exhibited well-defined layered structures (Fig. 2e), indicating sufficient structural stability during 2-day growth to introduce spatial patterns. Under prolonged incubation, the change in layer sharpness remained negligible for 5 days and became noticeable on day 7. After 28 days, the peak-to-valley ratio of the bands still retained about two-thirds of the original value. The results confirm the structural stability of FC1m crystals and support their use for programming spatial heterogeneity.

The JF-dye patterns exemplify the spatially programmed immobilization of cell-permeable organic ligands. To further evaluate programmability, we sequentially incubated crystal-growing cells with three spectrally distinct JF dyes in a defined order (Fig. 2i). By incrementally varying the incubation time from 1 to 5 h, we generated 11 sharp bands with ~100–200 nm bandwidths, equivalent to ~3.5–7 lattice periods (Fig. 2j–l). This sharpness arises from the fast labelling kinetics of JF dyes[34] (Supplementary Fig. 10) and low cytoplasmic equilibrium concentration of HaloTag-labelled building blocks. The former enables instant labelling as the building blocks were synthesized, whereas the latter ensures that the building blocks labelled with the previous dye depleted rapidly after dye switch. Among tested HaloTag fusion sites, the N terminal of FC1m-A affords the lowest cytosolic equilibrium concentration and thus is optimal for producing sharp bands (Extended Data Fig. 5).

Programmable immobilization of diverse materials

Sequential staining offers a viable route for the programmed immobilization of distinct organic molecules, where fluorophores could be readily replaced with other membrane-permeable, non-toxic molecules for spatially programmed immobilization in crystals. However, its limited molecular scope restricts broader application, motivating a modular platform for immobilizing virtually any guest material that fits within the crystal pores.

https://doi.org/10.1038/s41565-026-02198-x

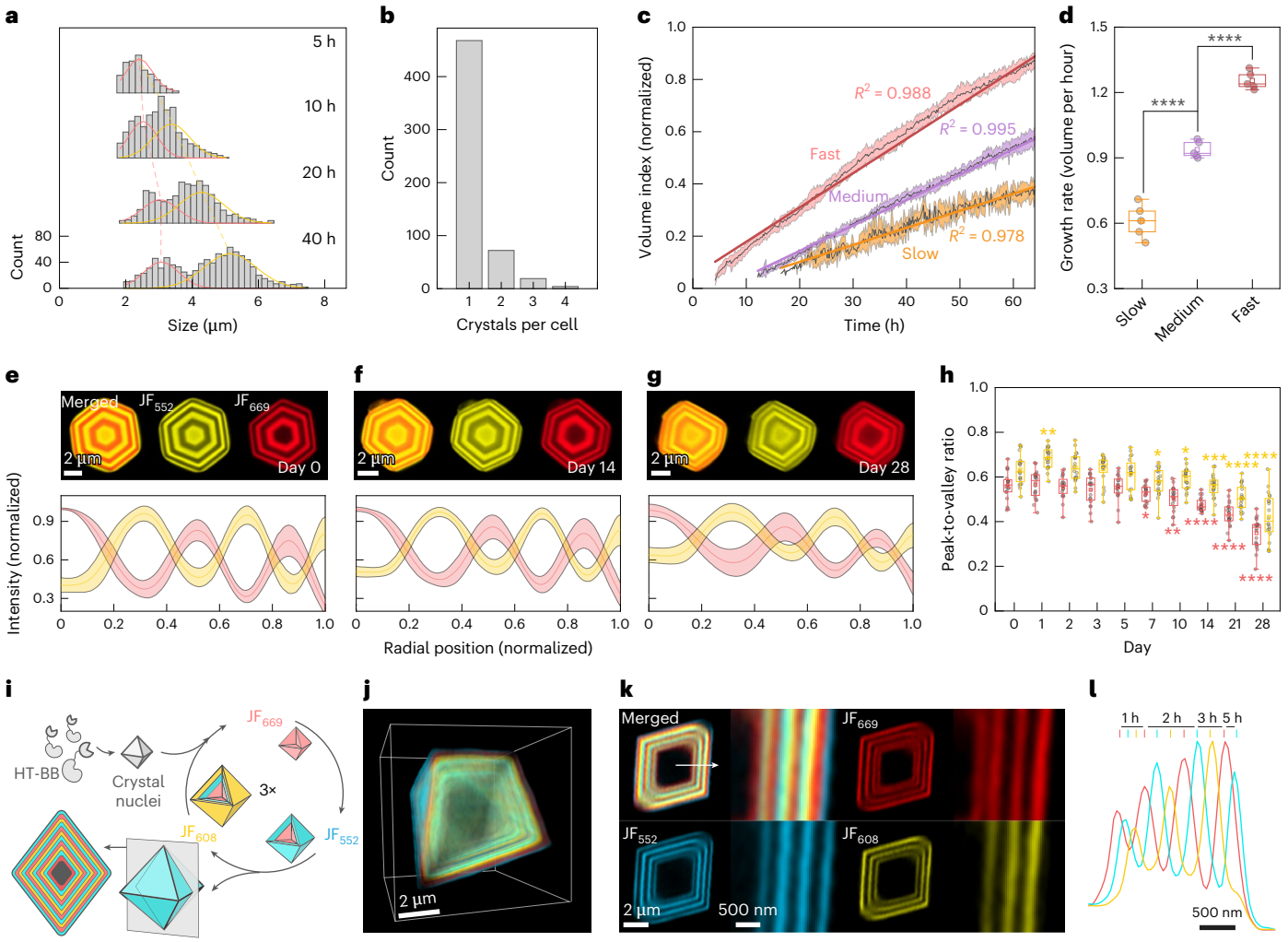

Fig. 2 | Characterization of intracellular FC1m crystals. a, Evolution of the size distribution of intracellular FC1m crystals. A bimodal distribution emerges approximately 10 h after induction. The size is approximated by the square root of the 2D segmented area. **b**, Statistical analysis of the number of crystals nucleated per cell. **c**, Growth profiles and corresponding simulations of three clonal HEK293T cell lines engineered to grow intracellular FC1m at fast (red), medium (violet) and slow (orange) rates. Shaded areas: s.d. Data are presented as mean ± s.d. $N = 5$ time-lapse sessions per group. **d**, Statistical comparison of the growth rates among the three clonal cell lines. Box bounds, the 25th/75th percentiles; whiskers, minimum/maximum; squares, mean; centre lines, median. $N = 5$ time-lapse sessions per group. Significance was determined using one-way analysis of variance test followed by Tukey's multiple-comparisons test. All tests were two-sided. ****$P < 0.0001$. **e**–**g**, Representative crystals (top) and their normalized fluorescence intensity profiles (bottom) showing the sharpness of colour transitions at days 0 (**e**), 14 (**f**) and 28 (**g**) after crystal harvest. Data are presented as mean ± s.d. (shaded areas). $N = 20$ crystals per condition. **h**, Statistical analysis of the evolution of band sharpness over varying incubation durations. The P values represent the comparison with the peak-to-valley ratio on day 0. Box bounds, the 25th/75th percentiles; whiskers, minimum/maximum; squares, mean; centre lines, median. $N = 20$ crystals per condition, Welch's t-test. All tests were two-sided. *$P < 0.05$, **$P < 0.01$, ***$P < 0.001$, ****$P < 0.0001$. **i**, Schematic of the sequential dye incubation protocol used to generate layered fluorescent patterns. HT-BB, HaloTag-labelled building block. **j**–**l**, Reconstructed 3D image (**j**), 2D cross-sectional image (**k**) and corresponding radial fluorescence profile (**l**) of a representative crystal obtained using the protocol in **i**.

To achieve this, we integrated HaloTag with orthogonal click chemistries to establish the guest-loading platform (Fig. 3a). 'Halo-Click' ligands containing both chloro- and click-reactive groups were designed and sequentially programmed into designated crystal layers, analogous to dye switching, after which extracted crystals can be loaded with guests bearing complementary click groups (Fig. 3b). Specifically, we synthesized four Halo-Click ligands: Cl-azide, Cl-dibenzocyclooctyne (DBCO), Cl-trans-cyclooctene (TCO) and Cl-methyltetrazine (mTz), designed for orthogonal strain-promoted azide–alkyne cycloaddition (SPAAC) and inverse electron-demand Diels–Alder reactions (Extended Data Fig. 6; Methods). Cell-permeability and HaloTag-labelling kinetics were jointly evaluated by ligand incubation at various concentrations and for different durations, followed by visualization using click-conjugated fluorophores (Supplementary Figs. 11 and 12). At ≥2 μM, all ligands labelled HaloTag within minutes, indicating efficient trans-membrane diffusion and HaloTag binding. Among them, the orthogonal Cl-TCO/Cl-azide pair showed the fastest labelling (Fig. 3c), consistent with band-sharpness results from sequential switching tests (Supplementary Figs. 13–16).

Next, we tested immobilization of diverse materials, including inorganic nanoparticles, proteins and organic molecules that fit the pore dimensions of FC1m (Supplementary Fig. 17). To facilitate visualization, we used fluorescent materials from each category, including quantum dots (QDs; Fig. 3e and Extended Data Fig. 7a–c), fluorescent proteins (FPs; Fig. 3f and Extended Data Fig. 7d) and fluorescent dyes (Fig. 3g), as proof of concept. We performed sequential switching between 2 μM Cl-TCO and Cl-azide in crystal-growing cell cultures at 8-h intervals for three cycles (Fig. 3d), followed by extraction of crystals and loading of the diverse materials. All three cargo types were

https://doi.org/10.1038/s41565-026-02198-x

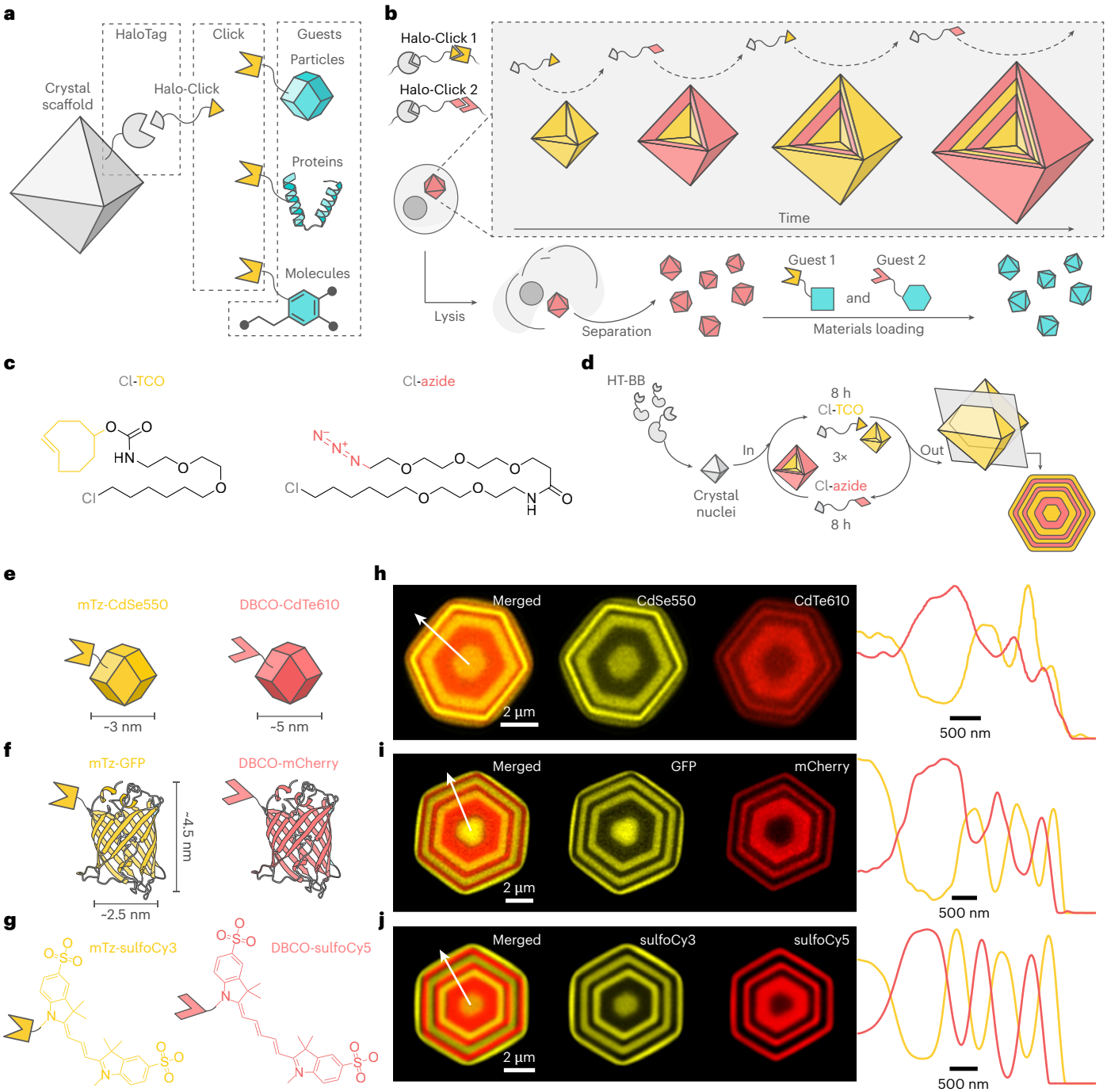

Fig. 3 | Materials immobilization and programmable synthesis of spatially patterned protein crystals. a, Schematic of Halo-Click chemistry for the modular immobilization of diverse nanomaterials into mesoporous FC1m crystals. **b**, Schematic of sequential incubation with orthogonal Halo-Click ligands to create spatially patterned crystals with layers of distinct chemistries. **c**, Structures of Halo-Click ligands Cl-TCO and Cl-azide synthesized for programmable functionalization. **d**, Schematic of the sequential incubation protocol used to generate spatially patterned architectures. **e**–**g**, Representative nanomaterials, including QDs (**e**), FPs (**f**) and fluorescent dyes (**g**), immobilized within the crystals programmed by the protocol described in **d**. **h**–**j**, Representative fluorescence images (left) and corresponding radial fluorescence profiles (right) of crystals loaded with QDs (**h**), FPs (**i**) and fluorescent dyes (**j**). Experiments were independently repeated three times with similar results.

immobilized in designated layers, whereas larger cargos with multivalent surface-clickable groups generally exhibit lower loading efficiency (Supplementary Fig. 18). While crystals may nucleate at different times, multilayer patterns are synchronized at the outermost layer. QD bands were slightly less sharp than protein and small-molecule bands, probably due to slow clearance of uncoupled QDs from solvent channels. Although HaloTag partially occupies pores and may hinder guest diffusion, this can be mitigated by tuning the HaloTag incorporation ratio and linker flexibility to balance pore accessibility with chemical-handle density and reduce pore blockage.

This programming strategy was further examined in other intracellular assemblies, including rod-shaped iPak4 and particle-shaped IC1[35,36] (Supplementary Fig. 19), both of which showed patterned structures along their growth axes. These results support the general

https://doi.org/10.1038/s41565-026-02198-x

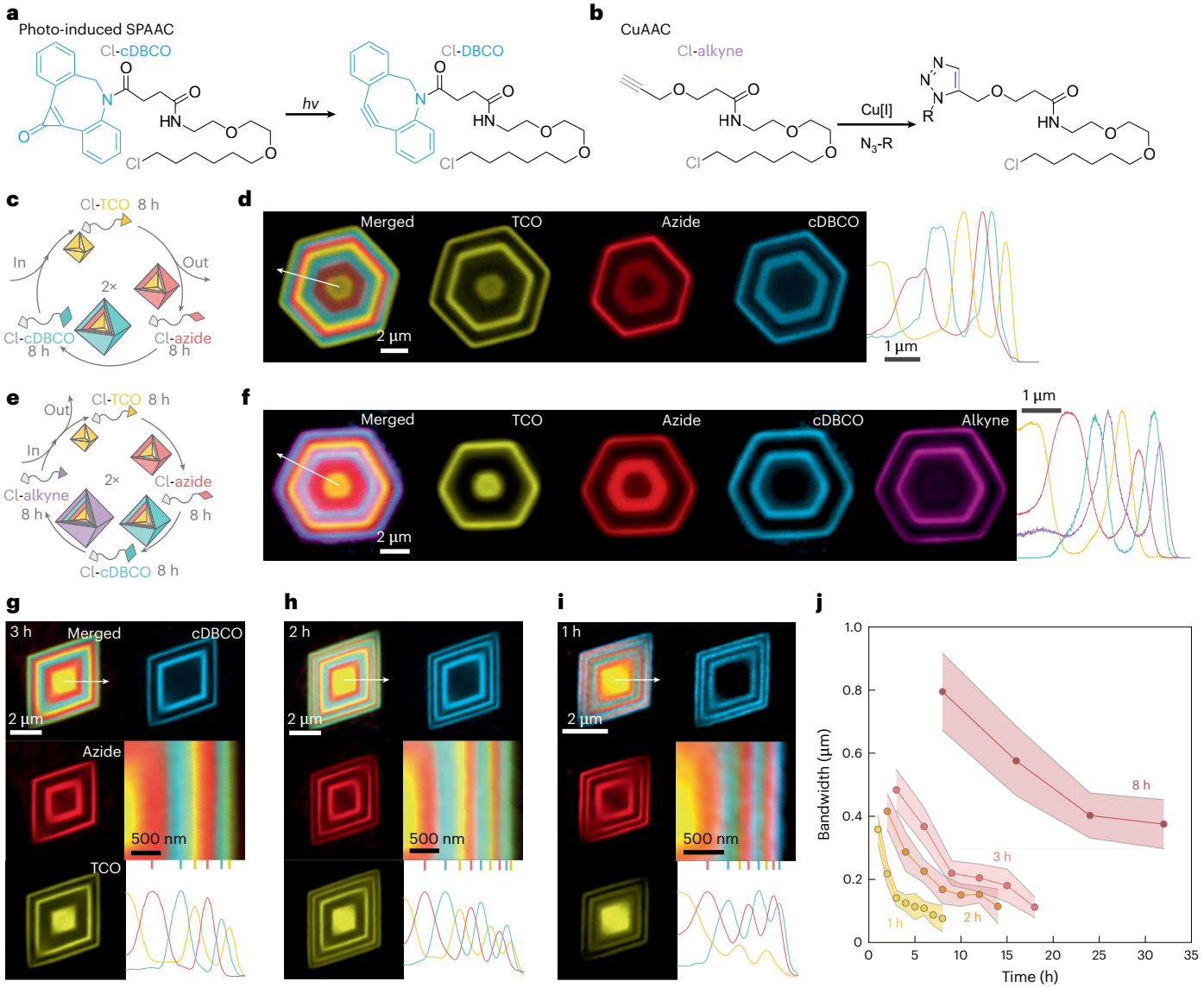

Fig. 4 | Expanding programmability by orthogonal inducible click chemistries. a, Photo-induced uncaging of cDBCO yields DBCO, enabling SPAAC. **b**, CuAAC reaction, requiring Cu(I) as the catalyst. **c**, Schematic of the programming protocol for introducing three chemically distinct layers into crystals. **d**, Representative crystal (left) and corresponding radial fluorescence profile (right) obtained using the protocol in **c**. **e**, Schematic of the programming protocol for introducing four chemically distinct layers into crystals. **f**, Representative crystal (left) and corresponding radial fluorescence profile (right) obtained using the protocol in **e**. **g**–**i**, Representative crystals (left) programmed using incubation intervals of 3 h (**g**), 2 h (**h**) and 1 h (**i**), along with their corresponding fluorescence profiles (right). **j**, Statistical analysis of the bandwidth as a function of time during switching for various intervals of 1–8 h. Data are presented as mean ± s.d. (shaded areas). $N = 20$ crystals derived from 4 independent biological replicates per group.

applicability of this approach for programmed synthesis of porous protein scaffolds.

Expanding programmability by orthogonal inducible click chemistry

To increase programming complexity beyond dual-material co-immobilization, we sought to incorporate more distinct guests by adding orthogonal conjugation chemistries. Beyond SPAAC and inverse electron-demand Diels–Alder, conditional reactions such as photo-triggered click chemistries[37,38] and copper-catalysed azide–alkyne cycloaddition (CuAAC)[39], offer conditional activation and minimal cross-reactivity, making them well suited for expanding programmability.

To explore this, we synthesized two additional Halo-Click ligands: Cl-cagedDBCO (cDBCO), a photo-activatable derivative for SPAAC[40] (Fig. 4a and Extended Data Fig. 8) and Cl-alkyne for CuAAC (Fig. 4b and Extended Data Fig. 8). Both showed rapid membrane crossing and HaloTag labelling (Supplementary Fig. 20) and were combined with Cl-TCO and Cl-azide to program up to four distinct material types.

We first tested three-band programming using Cl-TCO, Cl-azide and Cl-cDBCO, sequentially incubating cells with each ligand at 8-h intervals for two cycles (Fig. 4c). After programming, TCO- and azide-labelled layers were conjugated with sulfoCy3-mTz and sulfoCy5-DBCO, respectively; after washing, cDBCO were ultraviolet (UV)-deprotected and labelled with Alexa Fluor 488-azide. This yielded three bright, well-defined fluorescent bands, confirming spatial loading of three distinct materials (Fig. 4d). Replacing Cl-cDBCO with Cl-alkyne enabled similarly sharp third-band labelling via Cu(I)-catalysed CuAAC (Supplementary Fig. 21). Multiple switching sequences and incubation intervals further confirmed the robustness and versatility of photo-triggered and Cu(I)-catalysed click chemistries for spatial programming (Supplementary Figs. 21–23).

https://doi.org/10.1038/s41565-026-02198-x

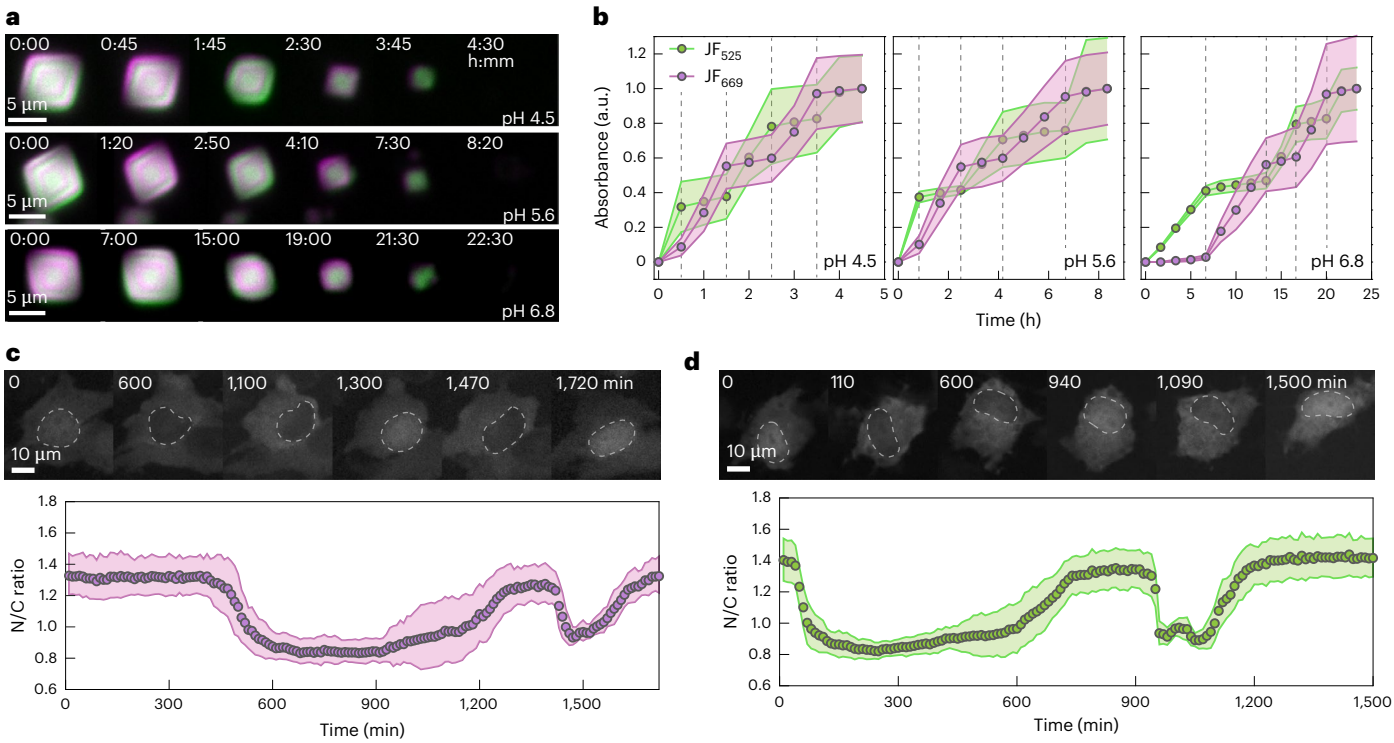

Fig. 5 | Sequential release of immobilized materials in physiological pHs. **a**, Key frames from time-lapse videos showing layer-by-layer dissolution of programmed crystals at pH 4.5 (top), 5.6 (middle) and 6.8 (bottom). **b**, Time-dependent release profiles of two immobilized dyes at pH 4.5 (left), 5.6 (middle) and 6.8 (right), showing gradual concentration increases during crystal dissolution. Data are presented as mean ± s.d. (shaded areas). $N = 3$ biological replicates per group. **c**,**d**, Time-dependent Akt signalling dynamics of HeLa cells incubated with pH 6.8 medium and FC1m-bFGF particles programmed into blank/bFGF (**c**) or bFGF/blank (**d**) patterns. Top: representative cells with oscillatory Akt signalling. Bottom: average nucleus-to-cytoplasm intensity ratio as a function of time. Data are presented as mean ± s.d. (shaded areas). $N = 15$ cells derived from 3 independent biological replicates per group.

We then extended the platform to co-immobilize four distinct materials by sequentially programming crystals with Cl-TCO, Cl-azide, Cl-cDBCO and Cl-alkyne at 8-h intervals for two cycles (Fig. 4e). After extraction, TCO-, azide-, alkyne- and cDBCO-modified layers were sequentially labelled with sulfoCy3-mTz, sulfoCy5-DBCO, Alexa Fluor 488-azide via CuAAC, and Cy3.5-azide after UV deprotection, respectively. The resulting crystals displayed four distinct bands with negligible crosstalk, each precisely matching the programmed sequence (Fig. 4f). To further assess band-width tunability, we varied ligand-switching intervals and found that sharp bands persisted at reduced intervals of 3, 2 and 1 h, with the thinnest bands reaching sub-100-nm resolution (Fig. 4g–i). Bandwidth scaled with the switching interval and matched the crystal growth profile (Fig. 4j).

Together, these results show that multiple orthogonal click chemistries enable complex and programmable spatial immobilization of diverse materials, offering unparalleled flexibility and versatility for patterning material distributions within the mesoporous scaffolds.

Sequential release of immobilized materials

One promising application of the spatially programmed FC1m crystals is sequential release of immobilized drugs. To test this, we investigated whether programmed crystals undergo controlled, layer-by-layer dissolution in physiologically relevant fluids. As a model, FC1m crystals were sequentially labelled with JF_{525} and JF_{669} dyes at 8-h intervals, generating five distinct layers for dissolution studies.

To simulate physiological environments, we imaged crystal dissolution in buffers with physiological ionic strength and pH 4.5–6.8, representing conditions in different tissues and organs[41]. As expected, dissolution proceeded in reverse programmed order at all tested pH values. Lower pH accelerated dissolution, with total dissolution time ranging from ~4.5 h at pH 4.5 to ~24 h at pH 6.8 (Fig. 5a). To assess dissolution at the population level, we monitored supernatant fluorescence during dissolution by UV–visible spectroscopy. Stepwise, alternating increases in JF_{525} and JF_{669} fluorescence indicates synchronized, layer-by-layer dissolution across the crystal population (Fig. 5b, Supplementary Fig. 24 and Supplementary Movie 3). This synchronization benefits from aligned outermost layers across crystals and a 'last-in, first-out' release scheme.

To demonstrate programmed biomolecular release, we loaded bFGF into designated programmed layers using the FP-loading protocol. Similarly, FC1m crystals were sequentially programmed into five distinct layers labelled with Cl-TCO and Cl-azide at 8-h intervals. Programmed crystals exhibited alternating layers carrying two distinct click-chemistry handles, but only one was conjugated to bFGF, generating two types of FC1m-bFGF pattern, with the outermost layer either containing or lacking bFGF (denoted as bFGF/blank and blank/bFGF, respectively). The fully dissolved particles contained 107.7 pg ml^{-1} bFGF (Supplementary Fig. 25). FC1m-bFGF particles were incubated with HeLa cells expressing a translocation biosensor for Akt activity (Akt-KTR) to monitor signalling in real time[42] (Fig. 5c,d). The culture medium was adjusted to pH 6.8. Both particle types induced oscillatory Akt signalling with activation patterns matching the programmed sequences (Fig. 5c,d) and fluorescent release kinetics under the same pH (Fig. 5a,b), whereas bFGF-free FC1m particles elicited negligible fluctuation in Akt signalling (Supplementary Fig. 26). It is noteworthy that the second activation window is consistently shorter, which may reflect slight pH drift during the experiment that alters the dissolution rate. Although release schedule and dose were not varied here, they could be tuned by altering the number or thickness of programmed layers and tuning handle density and cargo valency. Together, these results confirm the robust programmed release of biomolecules in a physiological setting and highlight

the potential of spatially engineered protein crystals for precision therapeutic applications.

Conclusion

Intracellular crystallization features several advantages as a platform for synthesizing mesoporous protein materials. Live cells provide a sustained intracellular supply of protein building blocks, which underlies the controllability and predictability of crystal synthesis. They also offer confined and reproducible microenvironments that naturally regulate and constrain nucleation and crystal dimensions, improving uniformity and scalability relative to synthetic microreactors[43]. In principle, this strategy is compatible with existing cell-factory infrastructure for industrial protein production, offering a potential path towards scalable synthesis[44]. Unlike many inorganic porous materials, such as metal–organic frameworks and mesoporous oxides that often require elevated temperatures, high pressures and/or specialized equipment[23,45], intracellular crystallization proceeds under physiological, ambient conditions and therefore enables real-time optical monitoring of crystal growth and provides facile control over the synthetic process. This study provides a strategy to spatially pattern materials at nanoscale, complementing existing methods such as nanolithography[46], DNA origami[47], 3D printing[48] and colloidal self-assembly[49].

Despite these advantages, the current platform still faces several limitations. First, crystal size uniformity is affected by continued cell division and fresh nucleation, which could be addressed by pausing the cell cycle during synthesis or using high-throughput sorting to isolate crystals with defined sizes. Second, although HaloTag provides a robust handle for chemical programming, it partially occupies pore volume and creates a trade-off between functionalization density and pore accessibility, particularly for larger cargos such as proteins and nanoparticles. Future optimization could tune the fraction of HaloTag-fused building blocks, engineer longer or more flexible linkers, use smaller self-labelling tags or adjust cargo-surface ligand density and valency to improve loading efficiency and uniformity. Third, while programmed crystals undergo layer-by-layer dissolution and sequential biomolecule release under physiological conditions, the released cargo remains covalently attached to the HaloTag-fused scaffold fragment. Although this did not impair bFGF-induced Akt signalling in this study, other applications may require traceless cargo release, which could be enabled by cleavable linkers responsive to pH, enzymes, redox state, light or other biological triggers.

Looking forward, several directions can further enhance the power and utility of the platform. First, expanding the crystal library through protein design and engineering remains a major goal. While we identified promising crystal candidates in this study through site-directed mutagenesis and individual screening, the process exhibits low throughput. Scalable platforms and directed evolution could greatly accelerate discovery. Second, reducing production costs will be essential for broader applications. While mammalian cells offer desirable features in this demonstration, alternative chassis such as bacteria or lower eukaryotes would be more cost-effective and provide microreactors with varied dimensions[50]. Third, innovations in programming modalities will be key to unlocking more complex material architectures. As the crystallization process is sensitive to subtle conformational changes, approaches that dynamically modulate protein conformation using physical cues, such as light or electromagnetic fields, could offer faster, more responsive and scalable programming. Finally, application-driven engineering of the programmed crystal synthesis platform represents another promising direction. In particular, the programmed materials are well suited for constructing multi-enzyme cascades to boost the efficiency of organic synthesis in vitro, as well as for organizing multistep metabolic pathways within living cells. Together, these innovations could further transform the intracellular crystallization platform and accelerate its practical applications for programmable materials synthesis.

Online content

Any methods, additional references, Nature Portfolio reporting summaries, source data, extended data, supplementary information, acknowledgements, peer review information; details of author contributions and competing interests; and statements of data and code availability are available at https://doi.org/10.1038/s41565-026-02198-x.

References

1. Hartje, L. F. & Snow, C. D. Protein crystal based materials for nanoscale applications in medicine and biotechnology. *WIREs Nanomed. Nanobiotechnol.* **11**, e1547 (2019).
2. Zhu, J. et al. Protein assembly by design. *Chem. Rev.* **121**, 13701–13796 (2021).
3. Luo, Q., Hou, C., Bai, Y., Wang, R. & Liu, J. Protein assembly: versatile approaches to construct highly ordered nanostructures. *Chem. Rev.* **116**, 13571–13632 (2016).
4. Kojima, M., Abe, S. & Ueno, T. Engineering of protein crystals for use as solid biomaterials. *Biomater. Sci.* **10**, 354–367 (2022).
5. Mikkila, J. et al. Janus-dendrimer-mediated formation of crystalline virus assemblies. *ACS Macro Lett.* **2**, 720–724 (2013).
6. Liljestrom, V., Seitsonen, J. & Kostiainen, M. A. Electrostatic self-assembly of soft matter nanoparticle cocrystals with tunable lattice parameters. *ACS Nano* **9**, 11278–11285 (2015).
7. Bailey, J. B. & Tezcan, F. A. Tunable and cooperative thermomechanical properties of protein–metal–organic frameworks. *J. Am. Chem. Soc.* **142**, 17265–17270 (2020).
8. Li, Z. et al. Accurate computational design of three-dimensional protein crystals. *Nat. Mater.* **22**, 1556–1563 (2023).
9. Sontz, P. A., Bailey, J. B., Ahn, S. & Tezcan, F. A. A metal organic framework with spherical protein nodes: rational chemical design of 3D protein crystals. *J. Am. Chem. Soc.* **137**, 11598–11601 (2015).
10. Laniado, J. & Yeates, T. O. A complete rule set for designing symmetry combination materials from protein molecules. *Proc. Natl Acad. Sci. USA* **117**, 31817–31823 (2020).
11. Huber, T. R., McPherson, E. C., Keating, C. E. & Snow, C. D. Installing guest molecules at specific sites within scaffold protein crystals. *Bioconjug. Chem.* **29**, 17–22 (2018).
12. Huber, T. R., Hartje, L. F., McPherson, E. C., Kowalski, A. E. & Snow, C. D. Programmed assembly of host–guest protein crystals. *Small* **13**, 1602703 (2016).
13. Nepal, M., Sheedlo, M. J., Das, C. & Chmielewski, J. Accessing three-dimensional crystals with incorporated guests through metal-directed coiled-coil peptide assembly. *J. Am. Chem. Soc.* **138**, 11051–11057 (2016).
14. Zhang, L., Bailey, J. B., Subramanian, R. H., Groisman, A. & Tezcan, F. A. Hyperexpandable, self-healing macromolecular crystals with integrated polymer networks. *Nature* **557**, 86–91 (2018).
15. Han, K., Zhang, Z. & Tezcan, F. A. Spatially patterned, porous protein crystals as multifunctional materials. *J. Am. Chem. Soc.* **145**, 19932–19944 (2023).
16. Korpi, A. et al. Self-assembly of electrostatic cocrystals from supercharged fusion peptides and protein cages. *ACS Macro Lett.* **7**, 318–323 (2018).
17. Lach, M., Strelow, C., Meyer, A., Mews, A. & Beck, T. Encapsulation of gold nanoparticles into redesigned ferritin nanocages for the assembly of binary superlattices composed of fluorophores and gold nanoparticles. *ACS Appl. Mater. Interfaces* **14**, 10656–10668 (2022).
18. Beyeh, N. K. et al. Crystalline cyclophane–protein cage frameworks. *ACS Nano* **12**, 8029–8036 (2018).
19. Välimäki, S. et al. Hierarchically ordered supramolecular protein-polymer composites with thermoresponsive properties. *Int. J. Mol. Sci.* **16**, 10201–10213 (2015).

20. Yang, H., Song, C. W., Lu, J. & Lin, D. In cellulo fabrication of supramolecular protein assemblies. *Chem. Rev.* **126**, 5585–5658 (2026).
21. Yan, Y. et al. Genetically encoded assembly recorder temporally resolves cellular history. *Nature* **652**, 1049–1059 (2026).
22. McPherson, A. & Gavira, J. A. Introduction to protein crystallization. *Acta Crystallogr.* **70**, 2–20 (2014).
23. Stock, N. & Biswas, S. Synthesis of metal–organic frameworks (MOFs): routes to various MOF topologies, morphologies, and composites. *Chem. Rev.* **112**, 933–969 (2012).
24. Kalikmanov, V. I. in *Nucleation Theory* (eds Beiglböck, W. et al.) 17–41 (Springer, 2012).
25. Nguyen, T. K. & Ueno, T. Engineering of protein assemblies within cells. *Curr. Opin. Struct. Biol.* **51**, 1–8 (2018).
26. Schönherr, R., Rudolph, J. M. & Redecke, L. Protein crystallization in living cells. *Biol. Chem.* **399**, 751–772 (2018).
27. Huang, P.-S., Boyken, S. E. & Baker, D. The coming of age of de novo protein design. *Chem. Soc. Rev.* **537**, 320–327 (2016).
28. Watson, J. L. et al. De novo design of protein structure and function with RFdiffusion. *Nature* **620**, 1089–1100 (2023).
29. Dauparas, J. et al. Robust deep learning–based protein sequence design using ProteinMPNN. *Science* **378**, 49–56 (2022).
30. Los, G. V. et al. HaloTag: a novel protein labeling technology for cell imaging and protein analysis. *ACS Chem. Biol.* **3**, 373–382 (2008).
31. Das, A. T., Tenenbaum, L. & Berkhout, B. Tet-on systems for doxycycline-inducible gene expression. *Curr. Gene Ther.* **16**, 156–167 (2016).
32. Gross, A. F., Sherman, E., Mahoney, S. L. & Vajo, J. J. Reversible ligand exchange in a metal–organic framework (MOF): toward MOF-based dynamic combinatorial chemical systems. *J. Phys. Chem. A* **117**, 3771–3776 (2013).
33. Grimm, J. B. et al. A general method to fine-tune fluorophores for live-cell and in vivo imaging. *Nat. Methods* **14**, 987–994 (2017).
34. Grimm, J. B. et al. A general method to optimize and functionalize red-shifted rhodamine dyes. *Nat. Methods* **17**, 815–821 (2020).
35. Lin, D. et al. Time-tagged ticker tapes for intracellular recordings. *Nat. Biotechnol.* **41**, 631–639 (2023).
36. Baskaran, Y. et al. An in cellulo-derived structure of PAK4 in complex with its inhibitor Inka1. *Nat. Commun.* **6**, 8681 (2015).
37. Kumar, G. S. & Lin, Q. Light-triggered click chemistry. *Chem. Rev.* **121**, 6991–7031 (2020).
38. Fu, Y., Simeth, N. A., Szymanski, W. & Feringa, B. L. Visible and near-infrared light-induced photoclick reactions. *Nat. Rev. Chem.* **8**, 665–685 (2024).
39. Hein, J. E. & Fokin, V. V. Copper-catalyzed azide–alkyne cycloaddition (CuAAC) and beyond: new reactivity of copper (I) acetylides. *Chem. Soc. Rev.* **39**, 1302–1315 (2010).
40. Poloukhtine, A. A., Mbua, N. E., Wolfert, M. A., Boons, G.-J. & Popik, V. V. Selective labeling of living cells by a photo-triggered click reaction. *J. Am. Chem. Soc.* **131**, 15769–15776 (2009).
41. Proksch, E. pH in nature, humans and skin. *J. Dermatol.* **45**, 1044–1052 (2018).
42. Maryu, G., Michiyuki, M. & Aoki, K. Multiplexed fluorescence imaging of ERK and Akt activities and cell-cycle progression. *Cell Struct. Funct.* **41**, 81–92 (2016).
43. Wang, L., Lee, M. H., Barton, J., Hughes, L. & Odom, T. W. Shape-control of protein crystals in patterned microwells. *J. Am. Chem. Soc.* **130**, 2142–2143 (2008).
44. Bachhav, B., de Rossi, J., Llanos, C. D. & Segatori, L. Cell factory engineering: challenges and opportunities for synthetic biology applications. *Biotechnol. Bioeng.* **120**, 2441–2459 (2023).
45. Zhao, T., Elzatahry, A., Li, X. & Zhao, D. Single-micelle-directed synthesis of mesoporous materials. *Nat. Rev. Mater.* **4**, 775–791 (2019).
46. Sharma, E. et al. Evolution in lithography techniques: microlithography to nanolithography. *Nanomaterials* **12**, 2754 (2022).
47. Dey, S. et al. DNA origami. *Nat. Rev. Methods Primers* **1**, 13 (2021).
48. Prabhakar, M. M., Saravanan, A., Lenin, A. H., Mayandi, K. & Ramalingam, P. S. A short review on 3D printing methods, process parameters and materials. *Mater. Today Proc.* **45**, 6108–6114 (2021).
49. Li, Z., Fan, Q. & Yin, Y. Colloidal self-assembly approaches to smart nanostructured materials. *Chem. Rev.* **122**, 4976–5067 (2021).
50. Tripathi, N. K. & Shrivastava, A. Recent developments in bioprocessing of recombinant proteins: expression hosts and process development. *Front. Bioeng. Biotechnol.* **7**, 420 (2019).

Methods

Design of protein crystals

The intracellular protein crystals were designed using the strategy we reported previously[11]. Protein cages with experimentally validated assembly structures were docked to form lattices in either the $F4_132$ (FC1 and FC2) or I432 (IC1) space group. Docking was carried out in PyMOL through alignment and translation operations. For the design of FC1 and FC2, two tetrahedral cages (TET-1 and TET-2) were first aligned such that each C2 symmetry axis coincided with the *x*, *y* and *z* coordinate axes, with the centre of mass positioned at the origin. TET-1 was held fixed, while TET-2 was rotated 90° about the *z* axis and translated along the [1, 1, −1] direction to dock with TET-1. The resulting D3-symmetric hexamer at the cage–cage interface was extracted and reoriented so that its C3 axis aligned with the *z* axis, its C2 axis aligned with the *x* axis, and its centre of mass remained at the origin. For the design of IC1, docking was performed between two octahedral cages (OCT-1 and OCT-2), where OCT-2 was translated relative to OCT-1 without applying any rotation. In both lattice types, the extracted D3 assembly unit contained the crystal contact and served as the input for Rosetta-based sequence design. Within the RosettaScripts framework, building blocks were symmetrized into D3 dihedrals, and interface distances were sampled by translating along the *z* axis (the dihedral axis) over a range of ±1.5 Å relative to the docked conformation, with no rotational degree of freedom. For each translation, the interface was designed using fixed backbones by rotamer packing with layer-based design constraints applied to interacting residues. Designs were then filtered using the following criteria: ddG <0, solvent-accessible surface area >200, clash score ≤2, and ≤2 unsatisfied hydrogen bonds, followed by visual inspection to confirm appropriate hydrophobic packing. The pore analysis of the designed crystals is performed using MAP_CHANNELS[51]. The pore size is defined by the diameter of the largest sphere that could traverse the crystal lattice in all directions. The porosity is defined by the solvent content in the lattice. The protein structures displayed in this work were rendered by PyMOL.

Library construction of mutated intracellular crystals. For the original intracellular FC1 crystals, the critical interfacial residues (T56 and I59 in the A chain) were first identified by inspecting the designed interface. Site-saturation mutagenesis was then employed to mutate these two sites. In brief, the Q5 Site-Directed Mutagenesis Kit (New England Biolabs, E0554S) was used. Mutagenic primers were manually designed following established design principles, with the degenerate NNK codon replacing the target sites. The resulting mutation library was transformed into an EndA- stable competent *Escherichia coli* strain (New England Biolabs, C3040H). Sixty colonies were picked and prepared to represent a broad coverage of possible mutants. Mutations were confirmed via Sanger sequencing. The libraries were screened for their crystallization capacity in HEK293T cells through transient transfection. The T55 site was screened first, while the T55R mutant was included in the subsequent screening of I58 mutations.

Cloning and molecular biology. To enable both transient transfection and the establishment of clonal cell lines, crystal-related genetic constructs were cloned into a PiggyBac vector (Addgene, 104454). Plasmid assembly was performed using the standard Gibson assembly protocol. Specifically, the vector backbone was linearized by double restriction enzyme digestion and purified using the GeneJET Gel Extraction Kit (Thermo Fisher Scientific, K0691). Target DNA inserts were amplified via polymerase chain reaction using the ProFlex PCR System (Thermo Fisher Scientific, 4484073) and assembled into the plasmid backbone through Gibson recombination. The rtTA3G and HaloTag sequences were obtained from Addgene plasmids #120309 and #177882, respectively. HaloTag was fused to the assembly constructs using a flexible 6×GGS peptide linker. All resulting plasmids were validated via full-length plasmid sequencing. The amino acid sequences of the proteins developed and used in this work are summarized in Supplementary Table 1.

Cell culture and transfection. HEK293T cells (ATCC, CRL-3216) were cultured and passaged according to established protocols, as previously reported[21,35]. Cells with fewer than ten passages were seeded at ~30% confluency in either 60-mm tissue culture dishes (STEMCELL Technologies, 38070) or 14-mm glass-bottom dishes (Cellvis, D35-14-1.5-N) pre-coated with 0.1 mg ml^{-1} poly-D-lysine (Sigma-Aldrich, P6407). Cells were maintained in Dulbecco's modified Eagle medium (DMEM; Corning, 15-017-CV) supplemented with 10% fetal bovine serum (VWR, 97068-104), 1% penicillin–streptomycin (Sigma-Aldrich, P4333) and 1% GlutaMAX Supplement (Thermo Fisher Scientific, 35050061), and incubated at 37 °C in a humidified 5% CO_2 atmosphere. When cell confluency reached 50–70%, transfection was performed using 25-kDa linear polyethyleneimine (Polysciences, 23966). After DNA introduction, cells were incubated under the same conditions for an additional 8–24 h before proceeding to downstream experiments.

SAXS characterization and analysis

Each solution containing intracellular crystals extracted and purified from cells (following the method reported in 'Isolation and purification of crystals' section) was loaded into a 1.5-mm-diameter quartz capillary, sealed with epoxy and shipped to the 12-ID-E beamline of the Advanced Photon Source at Argonne National Laboratory. For SAXS measurements at the beamline, an X-ray beam with a size of 0.2 mm (horizontal) × 0.1 mm (vertical) and an energy of 18 keV was irradiated onto the capillary. The diffraction signals from the sample were collected with a Pilatus 2M detector located at about 9 m downstream of the sample. The pixel size of this detector is 0.172 mm. Data were collected from various spots on each sample. Data processing was performed with the standard beamline data processing package available at the beamline. Reconstruction of electron density was performed with the Superflip software package[52].

Development of clonal HEK293T cell lines with stable FC1m expression. The PiggyBac transposon system was used to generate clonal HEK293T cell lines stably integrating the gene of interest. In brief, HEK293T cells were co-transfected with PiggyBac transposon plasmids encoding the target gene and a puromycin resistance marker, along with a Super PiggyBac transposase vector (NovoPro, V012800). Transfection was conducted using polyethyleneimine (1 mg ml^{-1}) as the delivery reagent. Forty-eight hours after transfection, cells were selected with 2 μg ml^{-1} puromycin (Gibco, A1113803), and antibiotic selection was maintained for 1–2 weeks to ensure stable integration. Clonal cell lines were established via limiting dilution, with individual cells seeded into 96-well plates and expanded after functional validation. Selected clones were preserved by either continuous passaging or cryogenic storage for future use.

Isolation and purification of crystals. Once crystal growth was complete, the culture medium was removed, and the cells were washed three times with PBS, each for 1 min. Subsequently, 2 ml of lysis buffer—comprising 0.1 M HEPES supplemented with 10% (v/v) NP40 (MP Biomedicals, 02198596-CF) and 10% (v/v) DNase (10 units μl^{-1}; GoldBio, D-300-1)—was added directly to each 60-mm cell culture dish. The cells were placed on a shaker at 70 rpm for 2 h to facilitate lysis. Afterwards, the crystal-containing suspension was transferred to a 1.5-ml microcentrifuge tube and centrifuged at 3,000*g* for 2 min. As crystals are denser, they pellet readily under the centrifugation condition, while most of the soluble impurities and cell debris stay in the supernatant. The supernatant was then discarded, and the crystal pellet was resuspended in 1 ml PBS, followed by another centrifugation at 3,000*g* for 2 min. This washing step was repeated twice to remove residual cellular debris. The final crystal pellet was resuspended in 1 ml

PBS for short-term storage (≤1 day), or in 1 ml storage buffer (see the preparation protocol in the Supplementary Methods) for long-term storage and structural stability tests (>1 day).

Because FC1m crystals are produced intracellularly and isolated from cell lysates, residual cellular components could, in principle, carry through purification. Such impurities may arise both from host materials retained within or between lattice domains during crystallization and from cellular debris that co-pellets with crystals during centrifugation-based separation. Consistent with this possibility, our measurements indicate that low but detectable levels of protein and nucleic-acid impurities remain in the purified FC1m crystal suspension obtained with the current workflow (Supplementary Fig. 27).

Programmable integration of Halo-Click ligands into defined crystal layers. HEK293T cells stably expressing FC1m were crystallized in the presence of 2 μg ml^{-1} DOX and 1 μM Halo-Click ligands at 37 °C, 5% CO_2. After 4 h, the medium was replaced with fresh DOX-containing medium supplemented with a different Halo-Click ligand, and incubation continued. Each ligand switch followed a standardized protocol.

Intervals between ligand switches were 1, 2, 3, 6 or 8 h. Examples of dual-ligand combinations include Cl-TCO/Cl-azide, Cl-TCO/Cl-DBCO, Cl-mTz/Cl-azide and Cl-mTz/Cl-DBCO. Three-ligand combinations include Cl-TCO, Cl-azide, and Cl-cDBCO; Cl-TCO, Cl-azide and Cl-alkyne; Cl-TCO, Cl-DBCO and Cl-cDBCO; and Cl-TCO, Cl-DBCO and Cl-alkyne. The four-ligand combination consists of Cl-TCO, Cl-azide, Cl-cDBCO and Cl-alkyne.

Immobilization of guest materials. For small-molecule guests, programmable assembly was performed on intracellular crystals. Following ligand integration, cells were washed 3× with PBS, fixed with 4% paraformaldehyde (20 min), permeabilized with 0.1% Triton X-100 (2 h) and washed again. For crystals with two Halo-Click ligand types (for example, Cl-TCO/Cl-azide), cells were incubated with PBS containing 10 μM mTz-sulfoCy3 and 10 μM DBCO-sulfoCy5 for 6 h. This enabled incorporation of two distinct dyes into defined crystal layers. For three ligands (for example, Cl-TCO, Cl-azide and Cl-cDBCO), after Cy3 and Cy5 labelling, cells were washed and incubated in PBS with 10 μM azide-AF488 (Lumiprobe, 11830) and UV-irradiated (290–350 nm, 0.372 mW cm^{-2}, 30 min), followed by 6 h in the dark. For four ligands (Cl-TCO, Cl-azide, Cl-cDBCO and Cl-alkyne), after Cy3, Cy5 and AF488 incorporation, cells were incubated with 20 μM CuBr, 200 μM sodium L-ascorbate and 10 μM azide-sulfoCy3.5 in PBS for 24 h, achieving four-dye labelling. For larger guests such as QDs and FPs, immobilization was conducted after crystal purification. The same labelling protocol was followed, with additional washing and centrifugation steps (3,000*g* for 2 min) to remove unbound materials.

Dissolution experiment. Following programmable assembly with JF525 and JF669 (JF525 8 h → JF669 16 h → JF525 24 h → JF669 24 h → JF525 24 h), crystals were isolated from HEK293T cells and resuspended in 1 ml PBS (pH 7.5), and 2-μl aliquots were placed on eight-chambered cover glass (CellVis, C8-1.5P). After partial PBS evaporation, samples were sealed with 0.3% agarose. Chambers were then filled with PBS (pH 6.8) and acetate buffer (pH 5.6 or 4.5), and imaged over time at 37 °C using wide-field epifluorescence microscopy. For bulk dissolution studies, crystals from 100-mm dishes were incubated in 100 ml PBS (pH 6.8, 37 °C) for 100 min. After centrifugation (3,000*g*, 5 min), supernatants were filtered through 100-kDa and then 10-kDa molecular weight cut-off filters, and concentrated to 2 ml. Similar experiments were conducted at varying timepoints (up to 1,400 min) in PBS (pH 6.8) and acetate buffer (pH 5.6 or 4.5). Absorbance spectra were measured with a spectrophotometer (Agilent Cary), and peaks at ~525 nm and ~669 nm were used to monitor fluorophore release.

Programmed Akt activation

Crystals with programmed sequences were extracted and purified from HEK293T cells. Surface-functionalized bFGF (mTz-bFGF or DBCO-bFGF, 50 μl) was then individually loaded onto the programmed Cl-TCO/Cl-azide crystals following the method described above. Human bFGF (Ala135-Ser288) was utilized in this study (GenScript, Z03116). After the assembly, unbound bFGF was removed by washing with PBS three times. HeLa cells were seeded on glass-bottom dishes and transfected with pCAGGS-Akt-FoxO3a-KTR-EGFP (Addgene, #125131) for monitoring Akt dynamics. Eight hours after transfection, the culture medium was replaced with 500 μl of imaging medium (FluoroBrite DMEM (Gibco A1896701) supplemented with 0.2% (vol/vol) fetal bovine serum and 1% (vol/vol) L-glutamine), and HeLa cells were further incubated for 6 h to allow Akt kinase activity to reach steady state. Subsequently, the medium was replaced with 500 μl of imaging medium with pH 6.8, into which 10 μl of programmed crystal loaded with bFGF was added, and time-lapse imaging was performed at 37 °C using a wide-field microscope (Zeiss Observer 7) to monitor Akt-dependent nucleocytoplasmic fluorescence shuttling.

Confocal imaging. Imaging was performed using fluorescence (Olympus IX81; Zeiss Axio Observer) and confocal microscopes (Zeiss LSM780, LSM980). Excitation lasers included 405 nm (4′,6-diamidino-2-phenylindole), 488 nm (JF525, AF488 and GFP), 561 nm (JF552, sulfoCy3, sulfoCy3.5, mCherry and CdSe550) and 633 nm (JF669, sulfoCy5 and CdTe610). Airyscan mode (LSM980) was used for crystals labelled with ≤3 fluorophores, whereas Lambda scan mode (LSM780) was used for samples labelled with four fluorophores. Hyperspectral imaging was captured using a 32-channel QUASAR detector (410–695 nm) and processed with Zeiss Zen Blue's linear unmixing. Reference spectra were collected under identical settings.

Time-lapse imaging. Cells were cultured on eight-chambered cover glass and imaged on a wide-field epifluorescence microscope equipped with the Zeiss CO_2 Module S1, maintaining 37 °C and 5% CO_2. Definite Focus 3 was used for autofocus during acquisition.

Image processing and data analysis

Image processing was performed with Python, MATLAB and ImageJ. For tracking crowded crystals, a collective tracking pipeline was developed. Intensity thresholds were applied to suppress early-stage false positives. Crystal candidates were segmented using greyscale distance transform and local maxima detection. Region growing was constrained by estimated radii to prevent overlap. A size threshold removed small artifacts. Growth modelling was performed using a Gaussian mixture model, excluding frames with fewer than ten detections. Two Gaussian kernels were fitted per sequence to account for potential crystal growth post-cell division. As the segmentation determined the area of crystals' two-dimensional (2D) projection (A), the volume index (VI) was calculated by $\mathrm{VI} = A^{3/2}$, indicating the volume of crystals. For the analysis of Akt dynamics, cell nuclei were first segmented using the Segment Anything Model (SAM)[53], and cytoplasmic regions were defined by dilating 5 pixels outwards from each nucleus. The nuclear-to-cytoplasmic (N/C) ratio was calculated as the mean nuclear GFP intensity divided by the mean cytoplasmic GFP intensity.

Statistics and reproducibility

Sample sizes are indicated in the corresponding figure legends. No statistical methods were used to predetermine sample sizes, but our sample sizes are similar to those reported in previous publications[21]. Data collection and analysis were not performed blind to the conditions of the experiments. Statistical comparisons between two groups were performed using two-tailed Welch's t-tests. Differences were considered statistically significant at $P < 0.05$ (*$P < 0.05$, **$P < 0.01$, ***$P < 0.001$, ****$P < 0.0001$).

Reporting summary
Further information on research design is available in the Nature Portfolio Reporting Summary linked to this article.

Data availability
All data needed to evaluate the conclusions in the study are available in the article or its Supplementary Information. Source data are provided with this paper. These data are also available via GitHub at https://github.com/DCLinLab/Programmed_crystal_synthesis.

References

51. Juers, D. H. & Ruffin, J. MAP_CHANNELS: a computation tool to aid in the visualization and characterization of solvent channels in macromolecular crystals. *J. Appl. Crystallogr.* **47**, 2105–2108 (2014).
52. Palatinus, L. & Chapuis, G. SUPERFLIP—a computer program for the solution of crystal structures by charge flipping in arbitrary dimensions. *Appl. Crystallogr.* **40**, 786–790 (2007).
53. Kirillov, A. et al. Segment anything. In *Proc. IEEE/CVF International Conference on Computer Vision* 4015–4026 (IEEE, 2023).

Acknowledgements
We thank L. D. Lavis and his team for providing JF dyes.

Author contributions
D.L. conceived of the project. D.L. and Y.L. cosupervised the project. H.Y. performed molecular biology, cell experiments and imaging. Y.Y., J.L., Y.W., C.W.S. and Y.S. contributed partially to cloning and imaging. D.-Z.L. and H.Y. synthesized the ligands. Z.L. and S.W. designed the crystals. B.L. performed SAXS. K.L. performed transmission electron microscopy characterization. Z.-H.Z. and H.Y. analysed the data. H.Y. and D.L. wrote the paper with input from all authors.

Funding
This work is supported by Department of Defense (DoD) Air Force Office of Scientific Research (AFOSR) Young Investigator Program (YIP) grant FA9550-23-1-0174 (D.L., H.Y. and Y.W.), National Institutes of Health (NIH) National Institute of General Medical Sciences (NIGMS) grant R35GM147274 (D.L., Y.Y., J.L. and Y.W.), National Science Foundation (NSF) Division of Materials Research (DMR) Award 2348276 (D.L. and Y.L.), David and Lucile Packard Foundation (D.L.), Kavli Neuroscience Discovery Institute Distinguished Graduate Fellowship (Y.Y.), the Howard Hughes Medical Institute (D.B.) and the Audacious Project at the Institute for Protein Design (Z.L., S.W. and D.B.). This paper used resources of the Advanced Photon Source, a US Department of Energy (DOE) Office of Science user facility at Argonne National Laboratory, and is based on research supported by the US DOE Office of Science-Basic Energy Sciences, under contract no. DE-AC02-06CH11357.

Competing interests
D.L. and H.Y. have filed a US patent application entitled 'Synthesis of protein particles'. The other authors declare no competing interests.

Additional information
Extended data is available for this paper at https://doi.org/10.1038/s41565-026-02198-x.

Supplementary information The online version contains supplementary material available at https://doi.org/10.1038/s41565-026-02198-x.

Correspondence and requests for materials should be addressed to Yayuan Liu or Dingchang Lin.

Peer review information *Nature Nanotechnology* thanks Tae Su Choi, Christopher Snow and Suppachai Srisantitham for their contribution to the peer review of this work. Peer reviewer reports are available.

https://doi.org/10.1038/s41565-026-02198-x

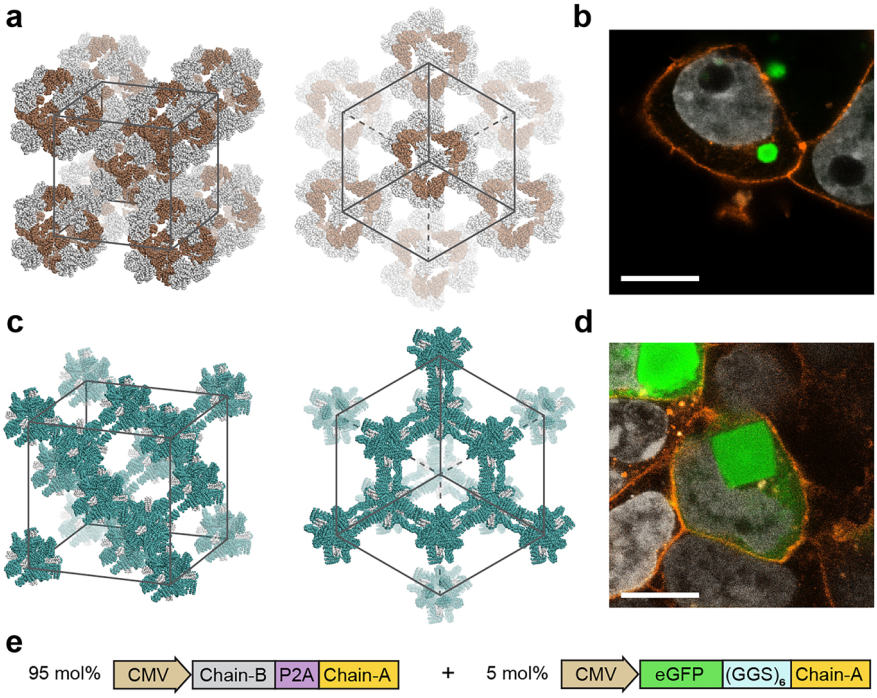

Extended Data Fig. 1 | Different variants of computationally designed intracellular crystals. (**a**) Perspective view (left) and [111] projection (right) of the IC1 crystal structure. (**b**) Fluorescence image showing the crystallization of IC1 in a HEK293T cell. (**c**) Perspective view (left) and [111] projection (right) of the FC2 crystal structure. (**d**) Fluorescence image showing the crystallization of FC2 in a HEK293T cell. Experiments were independently repeated 3 times with similar results. Scale bars: 10 μm. (**e**) DNA constructs for crystal screening via transient transfection.

https://doi.org/10.1038/s41565-026-02198-x

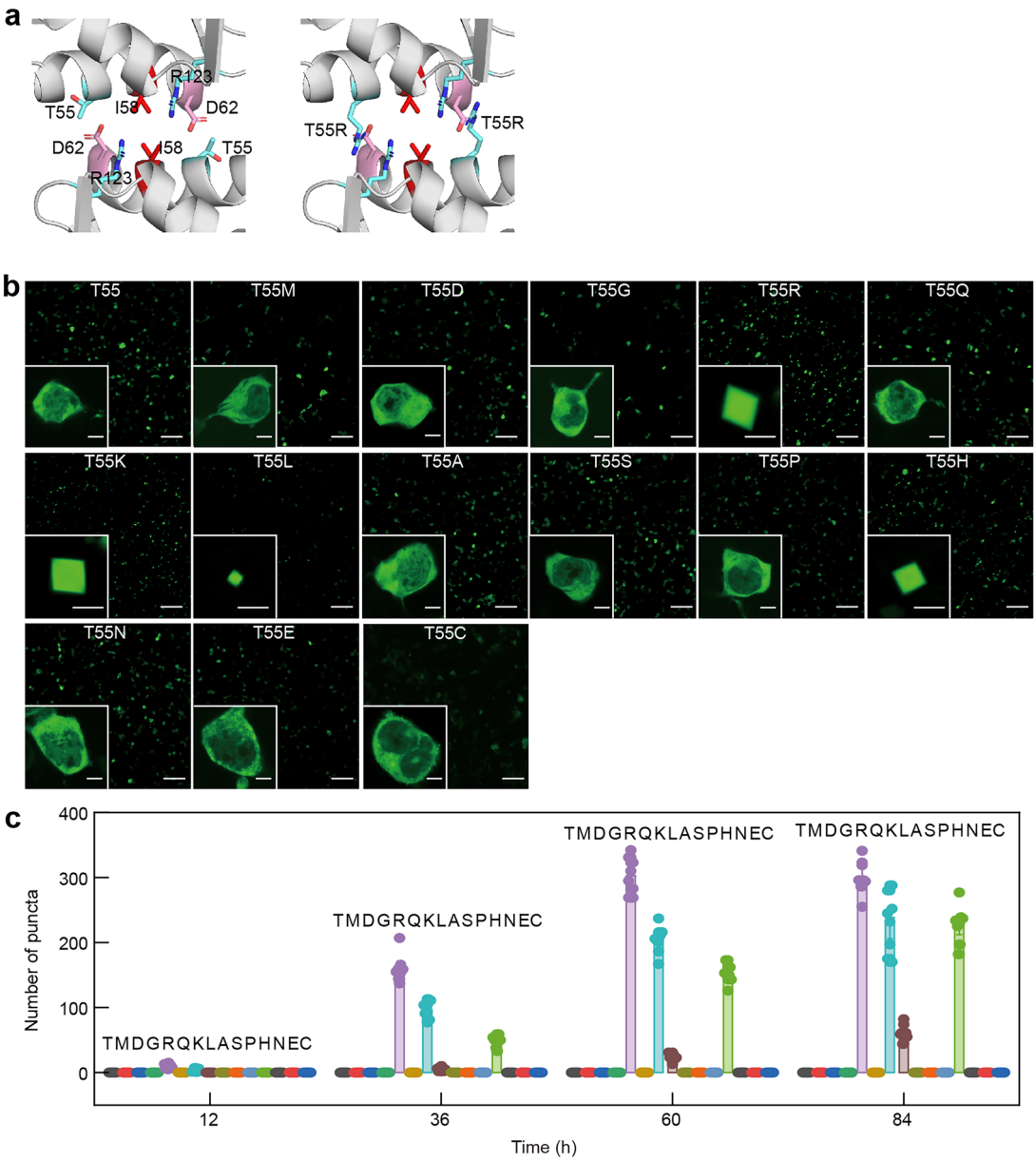

Extended Data Fig. 2 | Mutation of T55. (**a**) Comparison of the predicted interface with and without T55R mutation. The interface has a hydrophobic core of I58 and peripheral residues with hydrogen bonds. (**b**) Representative low-magnification and magnified (inset) images of different mutation variants at T55. Experiments were independently repeated 4 times with similar results. Scale bars: 100μm; 5 μm (inset). (**c**) Statistical comparison of the crystallization propensity of different variants. Intracellular crystallization was facilitated when T55 was mutated to positively charged amino acids histidine (H), arginine (R), and lysine (K), highlighting the critical role of electrostatic interaction with D62 for crystallization. Data are presented as mean ± s.e.m. N = 8 measurements derived from 4 independent biological replicates per group.

https://doi.org/10.1038/s41565-026-02198-x

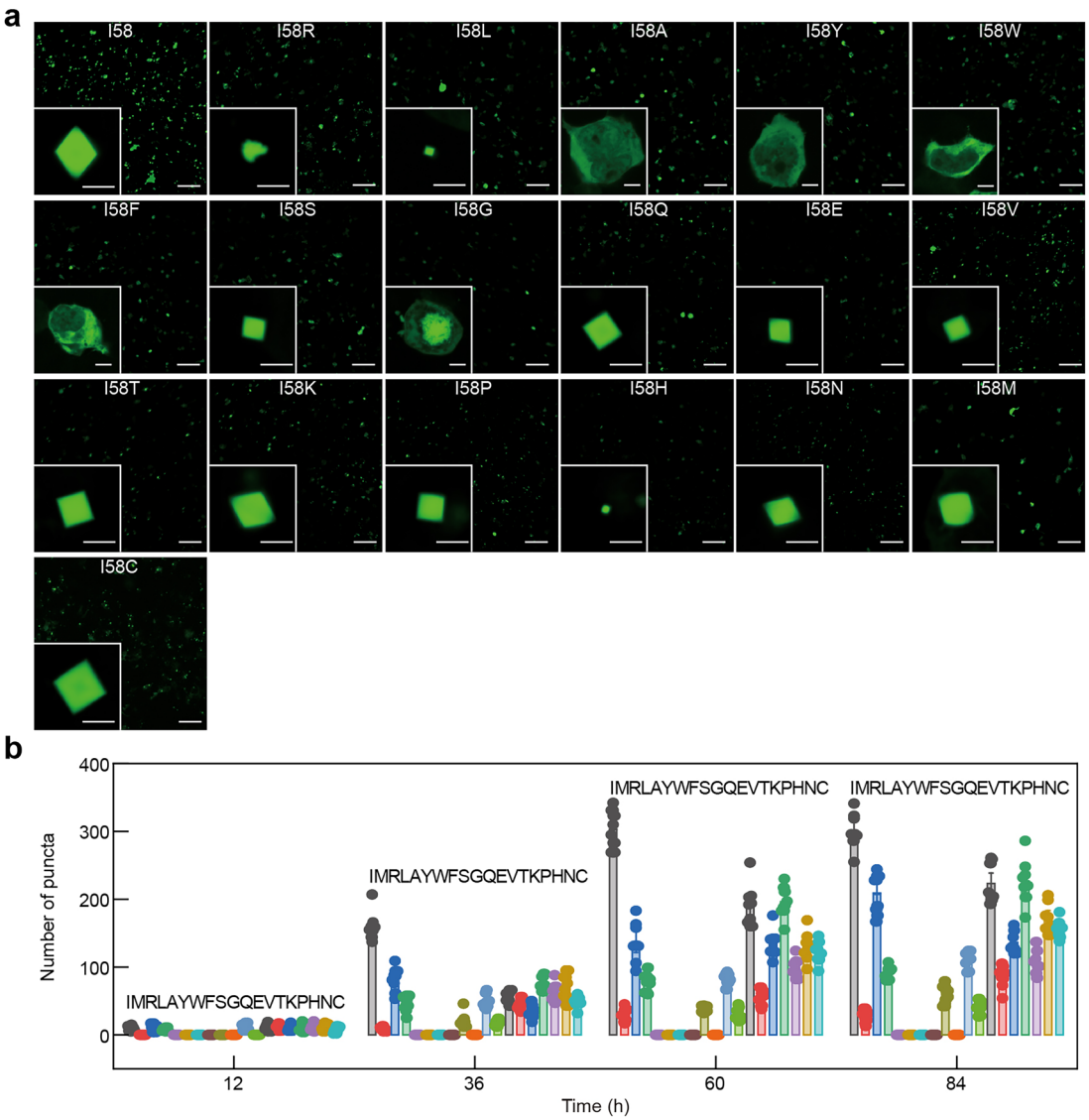

Extended Data Fig. 3 | Mutation of I58. (**a**) Representative low-magnification and magnified (inset) images of different mutation variants at the hydrophobic core I58. Experiments were independently repeated 4 times with similar results. Scale bars: 100μm; 5 μm (inset). (**b**) Statistical comparison of the crystallization propensity of different variants. Overall, intracellular crystallization was observed when a hydrophobic residue or cysteine is present at this site. Data are presented as mean ± s.e.m. N = 8 measurements derived from 4 independent biological replicates per group.

https://doi.org/10.1038/s41565-026-02198-x

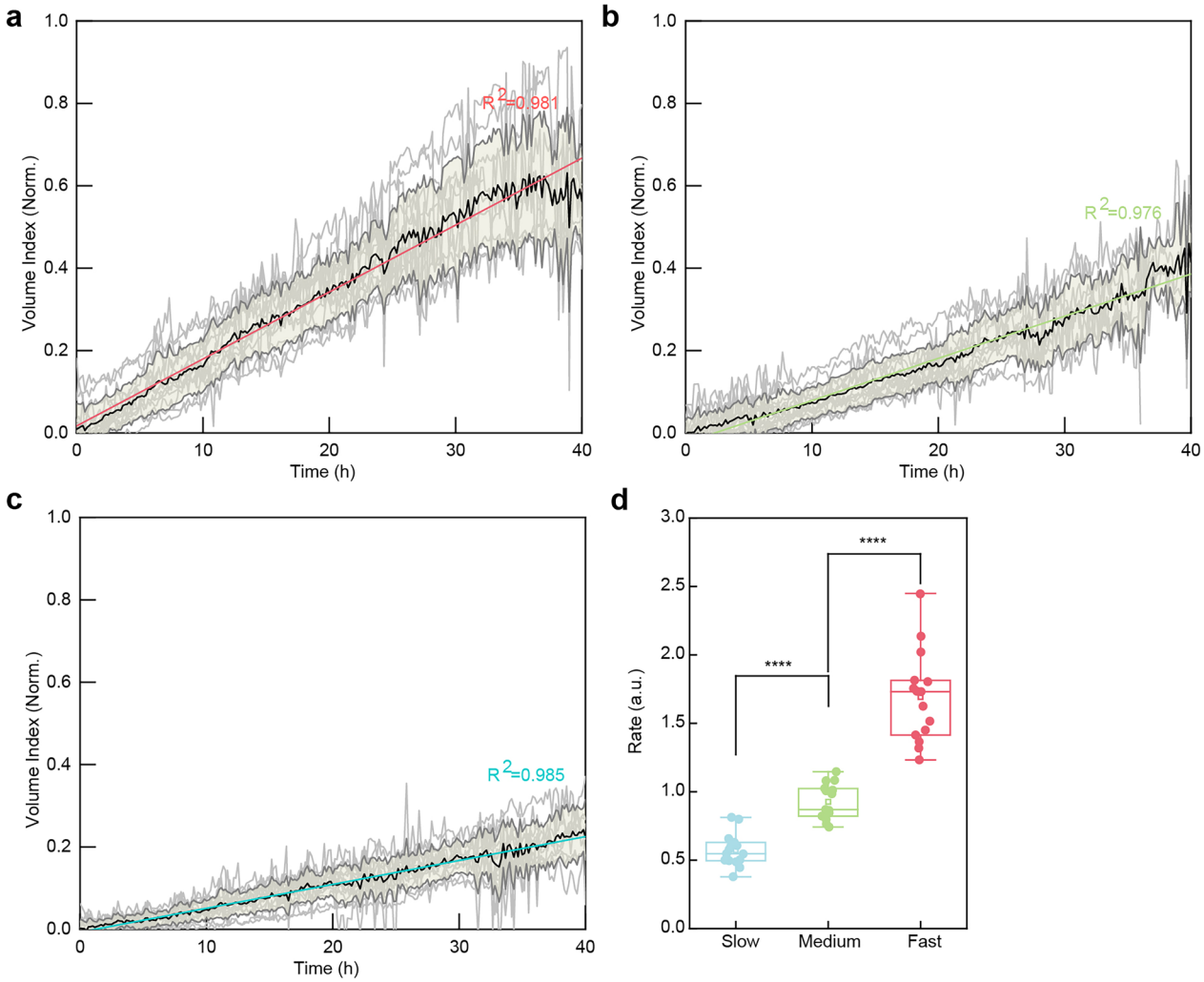

Extended Data Fig. 4 | Growth profiles obtained by single-crystal tracking. (**a-c**) The growth profiles of the FC1m crystals in the fast (**a**, N = 14 crystals), medium (**b**, N = 15 crystals), and slow (**c**, N = 15 crystals) cell lines. Data are presented as mean ± s.d. (shaded areas). (**d**) Statistical comparison of the growth rates of FC1m crystals within the three cell lines. N = 15 crystals per condition. ****: $p < 0.0001$, significance was determined using one-way ANOVA test followed by Tukey's multiple comparisons test. All tests were two-sided. Box bounds: the 25th/75th percentiles; whiskers: min/max; squares: mean; and center lines: median.

https://doi.org/10.1038/s41565-026-02198-x

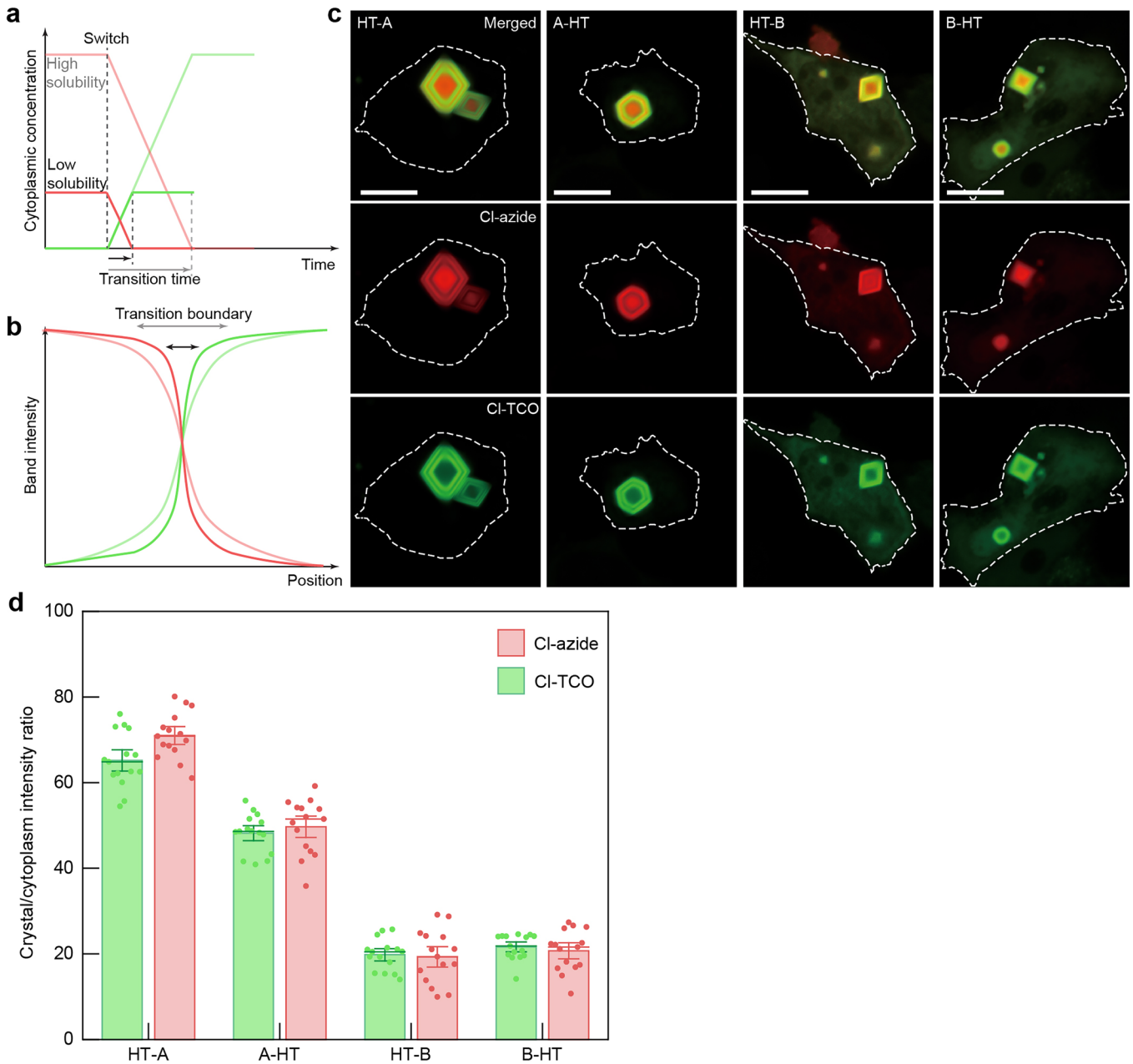

Extended Data Fig. 5 | The correlation between the band sharpness and cytoplasmic solubility of building blocks. (**a**,**b**) Plots showing how the cytoplasmic solubility determines the band sharpness. A lower solubility results in a shorter transition time after switching to the second band (**a**), therefore affording a sharper transition boundary (**b**). (**c**) Representative fluorescence images showing the solubility of FC1m crystals vary when HaloTag was fused to different terminals of the A and B building blocks, giving rise to varied band sharpness. Scale bars: 10 μm. (**d**) Statistical comparison of the crystal/cytoplasm intensity ratio with HaloTag fused to different terminals of A and B chains. Data are presented as mean ± s.e.m. N = 15 crystals derived from 3 independent biological replicates per group.

https://doi.org/10.1038/s41565-026-02198-x

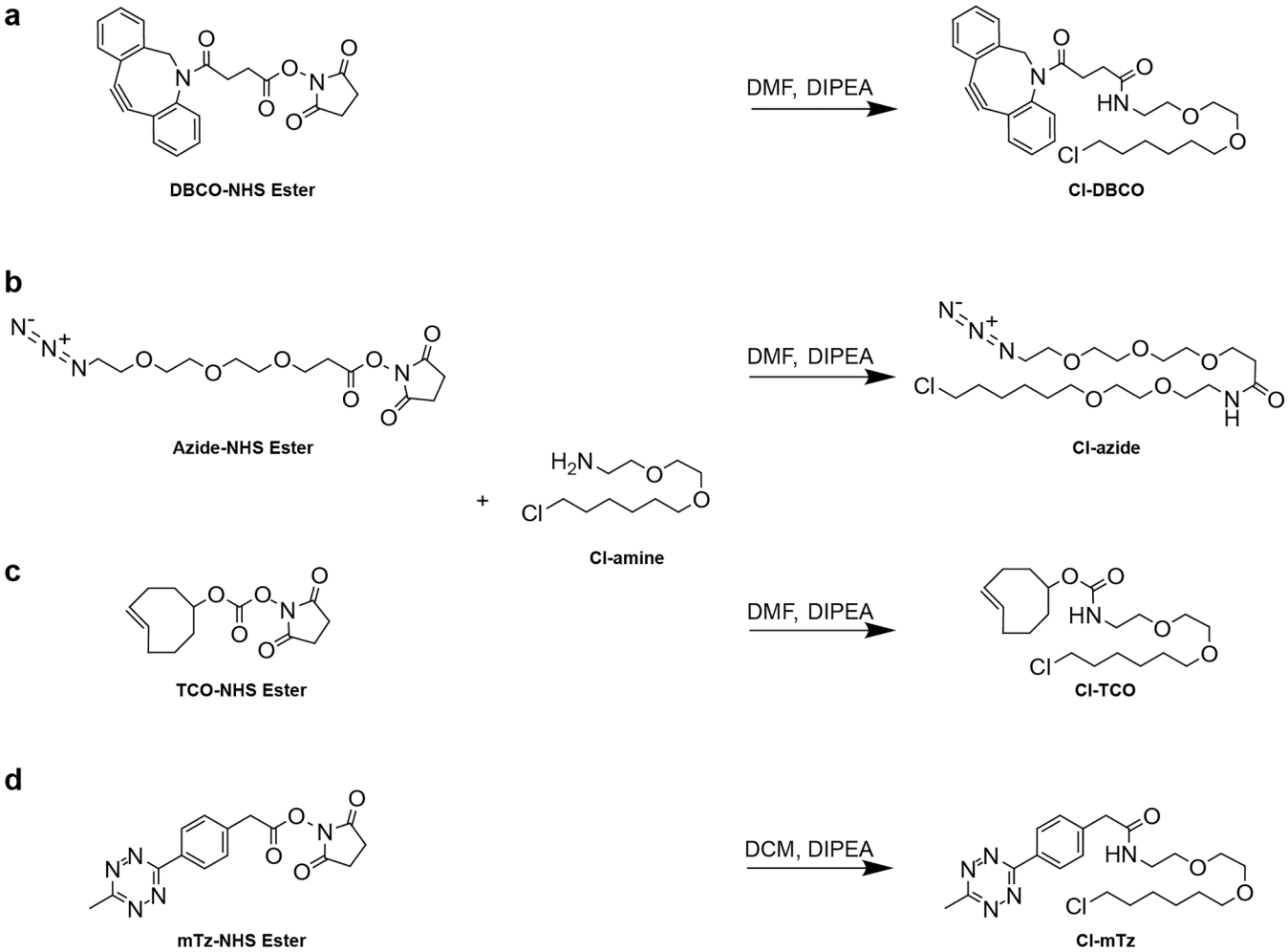

Extended Data Fig. 6 | Synthesis of Halo-Click ligands. (**a-d**) Synthetic routes for Cl-DBCO (**a**), Cl-azide (**b**), Cl-TCO (**c**), and Cl-mTz (**d**).

https://doi.org/10.1038/s41565-026-02198-x

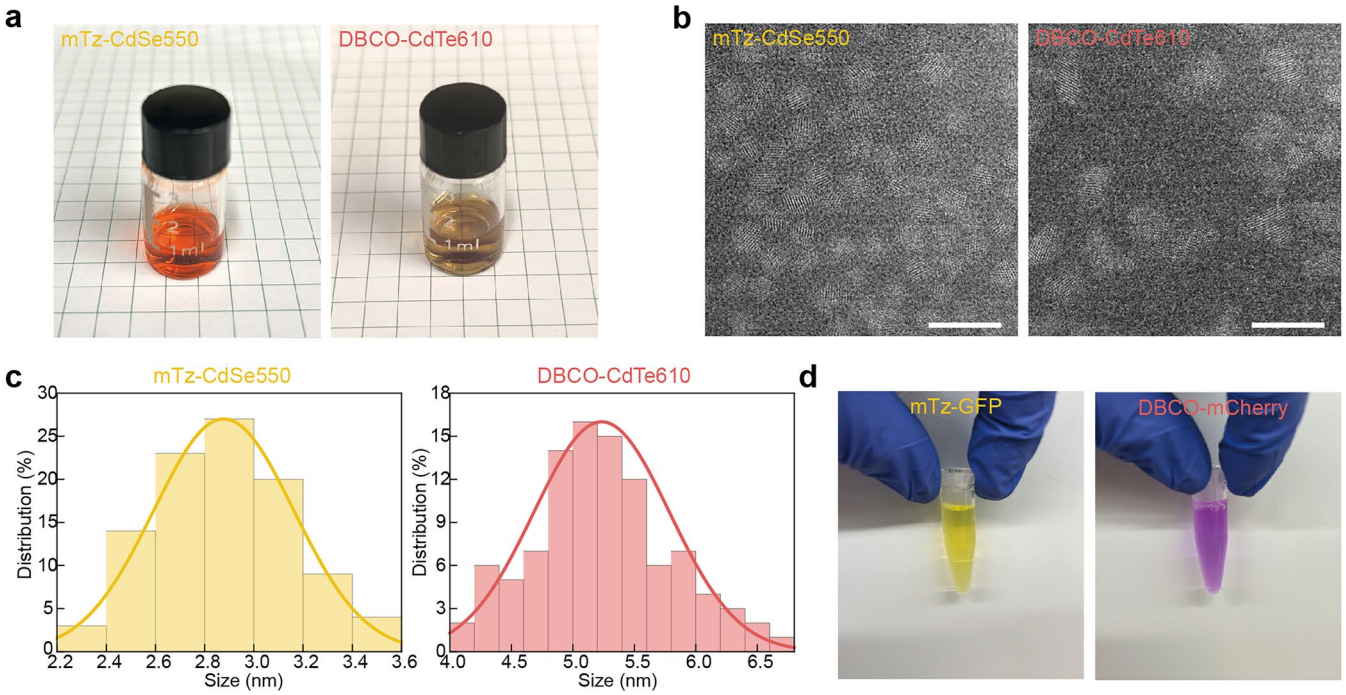

Extended Data Fig. 7 | Characterization of quantum dots and fluorescent proteins. (**a**) Photos of click-ligand modified quantum dots. (**b**) Transmission electron microscopy (TEM) images of the quantum dots. Scale bars: 10 nm. (**c**) Size distribution of quantum dots for immobilization. (**d**) Photos of click-ligand modified fluorescent proteins.

https://doi.org/10.1038/s41565-026-02198-x

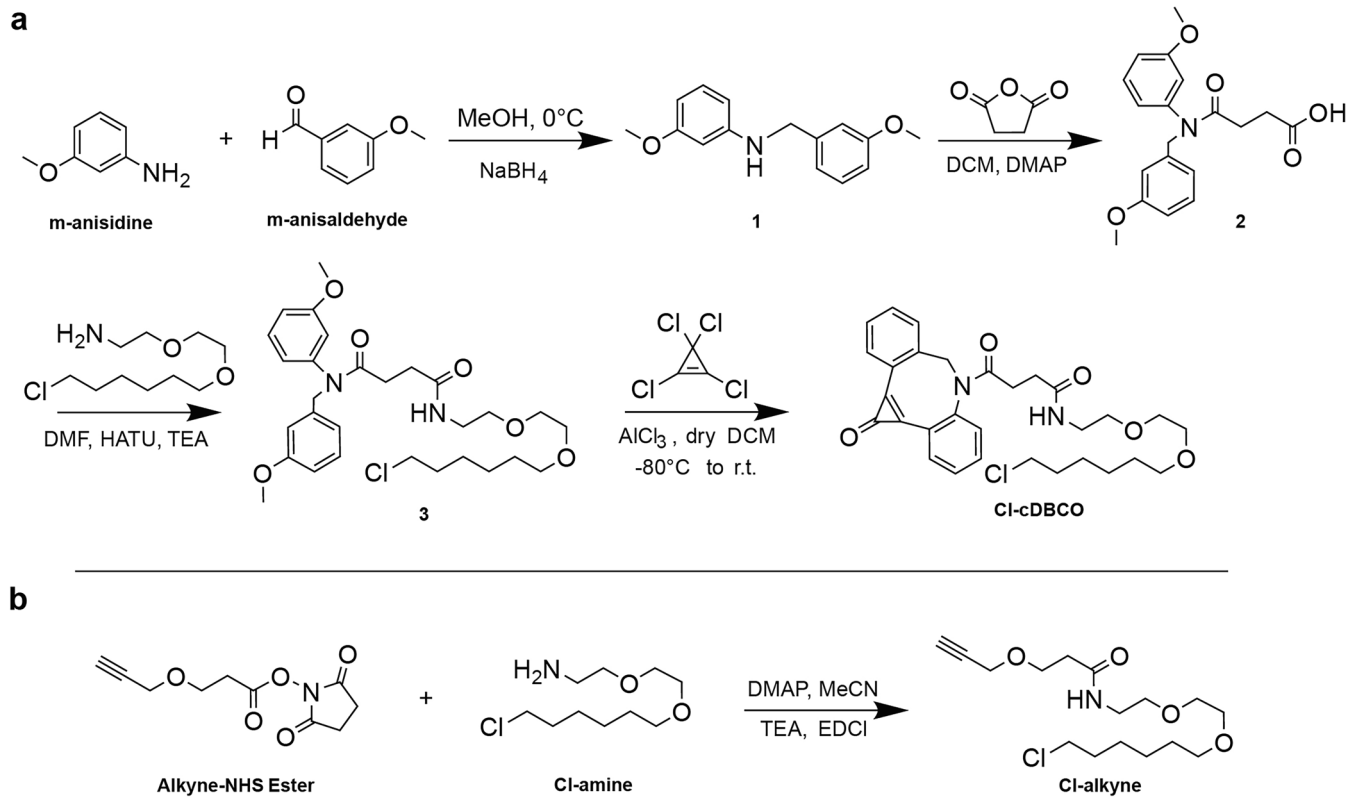

Extended Data Fig. 8 | Synthesis of Cl-cDBCO and Cl-alkyne. a,b Synthetic routes for Cl-cDBCO (**a**). and Cl-alkyne (**b**).

nature portfolio

Corresponding author(s): Dingchang Lin
Yayuan Liu

Last updated by author(s): Mar 18, 2026

Reporting Summary

Nature Portfolio wishes to improve the reproducibility of the work that we publish. This form provides structure for consistency and transparency in reporting. For further information on Nature Portfolio policies, see our Editorial Policies and the Editorial Policy Checklist.

Statistics

For all statistical analyses, confirm that the following items are present in the figure legend, table legend, main text, or Methods section.

n/a	Confirmed
☐	☒ The exact sample size (*n*) for each experimental group/condition, given as a discrete number and unit of measurement
☐	☒ A statement on whether measurements were taken from distinct samples or whether the same sample was measured repeatedly
☐	☒ The statistical test(s) used AND whether they are one- or two-sided *Only common tests should be described solely by name; describe more complex techniques in the Methods section.*
☒	☐ A description of all covariates tested
☒	☐ A description of any assumptions or corrections, such as tests of normality and adjustment for multiple comparisons
☐	☒ A full description of the statistical parameters including central tendency (e.g. means) or other basic estimates (e.g. regression coefficient) AND variation (e.g. standard deviation) or associated estimates of uncertainty (e.g. confidence intervals)
☐	☒ For null hypothesis testing, the test statistic (e.g. *F*, *t*, *r*) with confidence intervals, effect sizes, degrees of freedom and *P* value noted *Give P values as exact values whenever suitable.*
☒	☐ For Bayesian analysis, information on the choice of priors and Markov chain Monte Carlo settings
☒	☐ For hierarchical and complex designs, identification of the appropriate level for tests and full reporting of outcomes
☒	☐ Estimates of effect sizes (e.g. Cohen's *d*, Pearson's *r*), indicating how they were calculated

Our web collection on statistics for biologists contains articles on many of the points above.

Software and code

Policy information about availability of computer code

Data collection	We used Zeiss LSM780, LSM 800, LSM980 or Observer7 for data acquisition. The associated Zen Blue or Zen Black softwares (Zeiss) were used for data collection.
Data analysis	Linear spectral unmixing was performed using Zen Blue (Zeiss). Matlab (R2023a), Python (3.11), Pymol (3.1.0) and/or ImageJ were used for other data analyses. The code involved custom scripts comprising standard image processing steps, written for the specifics of the datasets, without any novel algorithms involved. Details of data analyses can be found in the manuscripts. Custom codes involved in data analysis can be found in our lab GitHub https://github.com/DCLinLab.

For manuscripts utilizing custom algorithms or software that are central to the research but not yet described in published literature, software must be made available to editors and reviewers. We strongly encourage code deposition in a community repository (e.g. GitHub). See the Nature Portfolio guidelines for submitting code & software for further information.

Data

Policy information about availability of data

All manuscripts must include a data availability statement. This statement should provide the following information, where applicable:

- Accession codes, unique identifiers, or web links for publicly available datasets
- A description of any restrictions on data availability
- For clinical datasets or third party data, please ensure that the statement adheres to our policy

All data needed to evaluate the conclusions in the study are available in the main manuscript or the supplementary materials. Source data is also deposited to GitHub at https://github.com/DCLinLab/Programmed_crystal_synthesis.

Research involving human participants, their data, or biological material

Policy information about studies with human participants or human data. See also policy information about sex, gender (identity/presentation), and sexual orientation and race, ethnicity and racism.

Reporting on sex and gender	*Use the terms sex (biological attribute) and gender (shaped by social and cultural circumstances) carefully in order to avoid confusing both terms. Indicate if findings apply to only one sex or gender; describe whether sex and gender were considered in study design; whether sex and/or gender was determined based on self-reporting or assigned and methods used. Provide in the source data disaggregated sex and gender data, where this information has been collected, and if consent has been obtained for sharing of individual-level data; provide overall numbers in this Reporting Summary. Please state if this information has not been collected. Report sex- and gender-based analyses where performed, justify reasons for lack of sex- and gender-based analysis.*
Reporting on race, ethnicity, or other socially relevant groupings	*Please specify the socially constructed or socially relevant categorization variable(s) used in your manuscript and explain why they were used. Please note that such variables should not be used as proxies for other socially constructed/relevant variables (for example, race or ethnicity should not be used as a proxy for socioeconomic status). Provide clear definitions of the relevant terms used, how they were provided (by the participants/respondents, the researchers, or third parties), and the method(s) used to classify people into the different categories (e.g. self-report, census or administrative data, social media data, etc.) Please provide details about how you controlled for confounding variables in your analyses.*
Population characteristics	*Describe the covariate-relevant population characteristics of the human research participants (e.g. age, genotypic information, past and current diagnosis and treatment categories). If you filled out the behavioural & social sciences study design questions and have nothing to add here, write "See above."*
Recruitment	*Describe how participants were recruited. Outline any potential self-selection bias or other biases that may be present and how these are likely to impact results.*
Ethics oversight	*Identify the organization(s) that approved the study protocol.*

Note that full information on the approval of the study protocol must also be provided in the manuscript.

Field-specific reporting

Please select the one below that is the best fit for your research. If you are not sure, read the appropriate sections before making your selection.

☐ Life sciences ☐ Behavioural & social sciences ☐ Ecological, evolutionary & environmental sciences

For a reference copy of the document with all sections, see nature.com/documents/nr-reporting-summary-flat.pdf

Life sciences study design

All studies must disclose on these points even when the disclosure is negative.

Sample size	*Describe how sample size was determined, detailing any statistical methods used to predetermine sample size OR if no sample-size calculation was performed, describe how sample sizes were chosen and provide a rationale for why these sample sizes are sufficient.*
Data exclusions	*Describe any data exclusions. If no data were excluded from the analyses, state so OR if data were excluded, describe the exclusions and the rationale behind them, indicating whether exclusion criteria were pre-established.*
Replication	*Describe the measures taken to verify the reproducibility of the experimental findings. If all attempts at replication were successful, confirm this OR if there are any findings that were not replicated or cannot be reproduced, note this and describe why.*
Randomization	*Describe how samples/organisms/participants were allocated into experimental groups. If allocation was not random, describe how covariates were controlled OR if this is not relevant to your study, explain why.*
Blinding	*Describe whether the investigators were blinded to group allocation during data collection and/or analysis. If blinding was not possible,*

Blinding | *describe why OR explain why blinding was not relevant to your study.*

Behavioural & social sciences study design

All studies must disclose on these points even when the disclosure is negative.

Study description	*Briefly describe the study type including whether data are quantitative, qualitative, or mixed-methods (e.g. qualitative cross-sectional, quantitative experimental, mixed-methods case study).*
Research sample	*State the research sample (e.g. Harvard university undergraduates, villagers in rural India) and provide relevant demographic information (e.g. age, sex) and indicate whether the sample is representative. Provide a rationale for the study sample chosen. For studies involving existing datasets, please describe the dataset and source.*
Sampling strategy	*Describe the sampling procedure (e.g. random, snowball, stratified, convenience). Describe the statistical methods that were used to predetermine sample size OR if no sample-size calculation was performed, describe how sample sizes were chosen and provide a rationale for why these sample sizes are sufficient. For qualitative data, please indicate whether data saturation was considered, and what criteria were used to decide that no further sampling was needed.*
Data collection	*Provide details about the data collection procedure, including the instruments or devices used to record the data (e.g. pen and paper, computer, eye tracker, video or audio equipment) whether anyone was present besides the participant(s) and the researcher, and whether the researcher was blind to experimental condition and/or the study hypothesis during data collection.*
Timing	*Indicate the start and stop dates of data collection. If there is a gap between collection periods, state the dates for each sample cohort.*
Data exclusions	*If no data were excluded from the analyses, state so OR if data were excluded, provide the exact number of exclusions and the rationale behind them, indicating whether exclusion criteria were pre-established.*
Non-participation	*State how many participants dropped out/declined participation and the reason(s) given OR provide response rate OR state that no participants dropped out/declined participation.*
Randomization	*If participants were not allocated into experimental groups, state so OR describe how participants were allocated to groups, and if allocation was not random, describe how covariates were controlled.*

Ecological, evolutionary & environmental sciences study design

All studies must disclose on these points even when the disclosure is negative.

Study description	*Briefly describe the study. For quantitative data include treatment factors and interactions, design structure (e.g. factorial, nested, hierarchical), nature and number of experimental units and replicates.*
Research sample	*Describe the research sample (e.g. a group of tagged Passer domesticus, all Stenocereus thurberi within Organ Pipe Cactus National Monument), and provide a rationale for the sample choice. When relevant, describe the organism taxa, source, sex, age range and any manipulations. State what population the sample is meant to represent when applicable. For studies involving existing datasets, describe the data and its source.*
Sampling strategy	*Note the sampling procedure. Describe the statistical methods that were used to predetermine sample size OR if no sample-size calculation was performed, describe how sample sizes were chosen and provide a rationale for why these sample sizes are sufficient.*
Data collection	*Describe the data collection procedure, including who recorded the data and how.*
Timing and spatial scale	*Indicate the start and stop dates of data collection, noting the frequency and periodicity of sampling and providing a rationale for these choices. If there is a gap between collection periods, state the dates for each sample cohort. Specify the spatial scale from which the data are taken*
Data exclusions	*If no data were excluded from the analyses, state so OR if data were excluded, describe the exclusions and the rationale behind them, indicating whether exclusion criteria were pre-established.*
Reproducibility	*Describe the measures taken to verify the reproducibility of experimental findings. For each experiment, note whether any attempts to repeat the experiment failed OR state that all attempts to repeat the experiment were successful.*
Randomization	*Describe how samples/organisms/participants were allocated into groups. If allocation was not random, describe how covariates were controlled. If this is not relevant to your study, explain why.*
Blinding	*Describe the extent of blinding used during data acquisition and analysis. If blinding was not possible, describe why OR explain why blinding was not relevant to your study.*

Did the study involve field work? ☐ Yes ☐ No

Field work, collection and transport

Field conditions	*Describe the study conditions for field work, providing relevant parameters (e.g. temperature, rainfall).*
Location	*State the location of the sampling or experiment, providing relevant parameters (e.g. latitude and longitude, elevation, water depth).*
Access & import/export	*Describe the efforts you have made to access habitats and to collect and import/export your samples in a responsible manner and in compliance with local, national and international laws, noting any permits that were obtained (give the name of the issuing authority, the date of issue, and any identifying information).*
Disturbance	*Describe any disturbance caused by the study and how it was minimized.*

Reporting for specific materials, systems and methods

We require information from authors about some types of materials, experimental systems and methods used in many studies. Here, indicate whether each material, system or method listed is relevant to your study. If you are not sure if a list item applies to your research, read the appropriate section before selecting a response.

Materials & experimental systems

n/a	Involved in the study
☒	☐ Antibodies
☐	☒ Eukaryotic cell lines
☒	☐ Palaeontology and archaeology
☒	☐ Animals and other organisms
☒	☐ Clinical data
☒	☐ Dual use research of concern
☒	☐ Plants

Methods

n/a	Involved in the study
☒	☐ ChIP-seq
☒	☐ Flow cytometry
☒	☐ MRI-based neuroimaging

Eukaryotic cell lines

Policy information about cell lines and Sex and Gender in Research

Cell line source(s)	HEK293T cells (ATCC, CRL-3216)
Authentication	The cell lines used were authenticated by the source and were not further authenticated.
Mycoplasma contamination	All cells were tested negative for mycoplasma.
Commonly misidentified lines (See ICLAC register)	No commonly misidentified cell lines were used in the study

Plants

Seed stocks	N/A
Novel plant genotypes	N/A
Authentication	N/A